
On convex conceptual regions in deep network representations

Lenka Tětková
lenhy@dtu.dk

Thea Brüsch
theb@dtu.dk

Teresa Karen Scheidt
tksc@dtu.dk

Fabian Martin Mager
fmager@dtu.dk

Rasmus Ørtoft Aagaard
s164419@student.dtu.dk

Jonathan Foldager
jonf@dtu.dk

Tommy Sonne Alstrøm
tsal@dtu.dk

Lars Kai Hansen
lkai@dtu.dk

Section for Cognitive Systems, DTU Compute,
Technical University of Denmark
2800 Kongens Lyngby, Denmark

Abstract

The current study of human-machine alignment aims at understanding the geometry of latent spaces and the correspondence to human representations. Gärdenfors' conceptual spaces is a prominent framework for understanding human representations. Convexity of object regions in conceptual spaces is argued to promote generalizability, few-shot learning, and intersubject alignment. Based on these insights, we investigate the notion of convexity of concept regions in machine-learned latent spaces. We develop a set of tools for measuring convexity in sampled data and evaluate emergent convexity in layered representations of state-of-the-art deep networks. We show that convexity is robust to basic re-parametrization, hence, meaningful as a quality of machine-learned latent spaces. We find that approximate convexity is pervasive in neural representations in multiple application domains, including models of images, audio, human activity, text, and brain data. We measure convexity separately for labels (i.e., targets for fine-tuning) and other concepts. Generally, we observe that fine-tuning increases the convexity of label regions, while for more general concepts, it depends on the alignment of the concept with the fine-tuning objective. We find evidence that pre-training convexity of class label regions predicts subsequent fine-tuning performance.

1 Introduction

Understanding the barriers to human-machine alignment is as important as ever (see, e.g., [10, 45]). Representational alignment is a first step towards a greater aim of understanding value alignment [17]. For the understanding of alignment, it is fundamental to establish a common language for regularities observed in human and machine representations. Here we motivate and introduce the concept of convexity of object regions in machine learned latent spaces.

Representational spaces in the brain can be described in several ways, for example, geometric psychological spaces informed by similarity judgments or, as based in the neurosciences, derived from the measurement of neural activity [5, 57]. Conceptual spaces proposed by Gärdenfors are a mature approach to the former, i.e., human-learned geometrical representations of semantic similarity

[32]. The geometrical approach is rooted in work by Shepard [54], who opens with the important observation: “Because any object or situation experienced by an individual is unlikely to recur in exactly the same form and context, psychology’s first general law should, I suggest, be a law of generalization”. This leads Shepard to favor geometrical representations in which concepts are represented by extended regions rather than single points, to allow for robust generalization. This is the view that has been comprehensively expanded and quantified by Gärdenfors and coworkers [32]. The cognitive science insights are complemented by extant work investigating alignment between learned representations in machine and human conceptual spaces [18, 37, 59], and numerous specific properties of the latent geometrical structure have been studied, such as the emergence of semantic separability in machine latent representations [46]. New insights in the representational geometry are found using the intrinsic dimension measure [59]. The relevant geometries are not necessarily flat Euclidean spaces, but often better described as general manifolds [40, 1]. In fact, Hénaff et al. [39] suggest that semantic separability emerges by flattening or straightening trajectories in latent spaces, such as was earlier proposed for machine representations [15]. Similar reasoning was crucial for early methodological developments like ISOMAP [58] and general kernel methods [48].

1.1 Convexity in conceptual spaces

Based on Shepard’s idea of objects as extended regions, Gärdenfors formulated the hypothesis that *natural* concepts form convex regions in human geometrical representations [30, 32, 63, 27]. Ströbner [55] elaborated on the notion of natural concepts as a social construct: “[Natural concepts] are often found in the core lexicon of natural languages—meaning that many languages have words that (roughly) correspond to such concepts—and are acquired without much instruction during language acquisition.” One way to interpret the naturalness notion is to link it to independent physical mechanisms with macroscopic effects, i.e., effects that will be visible to all, hence, likely to appear in joint vocabularies. Such independent mechanisms play a core role in causality [50]. A more low-level interplay between human and machine conceptual representations was discussed in [7] with a specific focus on grounding shape spaces. The work reports good correspondences between human shape representations as obtained by pairwise similarity judgments and machine representations of the shape obtained from supervised and unsupervised learning, however, without touching the question of the convexity of object regions in machines.

Convexity is closely related to generalization in cognitive systems [31, 33]. The defining property of convexity (see Definition 1) implies that categorization can be extended by interpolation. We also note that simple generalization based on closeness to prototypes leads to convex decision regions (Voronoi tessellation induces convex regions) [34]. Interestingly, convexity is also claimed to support few-shot learning [31]. When basic concepts are learned as convex regions, new labels can be formed by geometrically guided composition, leading to new convex regions (e.g., by conjunction) or by other inductions leading to sets of convex regions. Finally, it is claimed that convexity supports communication and interaction and thus the negotiation of meaning between subjects and the emergence of socially universal concepts, i.e., natural concepts [63].

The geometry-driven cognitive science insights motivate our investigation here: *Are generalizable, grounded concepts implemented as convex regions in machine-learned representations?*

In supervised learning, i.e., self-supervised pretraining followed by downstream fine-tuning, classification labels used as supervision signals clearly play a special role. We will carefully measure convexity for classes and other concepts separately in our experimental investigation.

The convexity of conceptual regions in machine-learned representations has not been addressed before, and we, therefore, first need to develop the required investigative tools. Our contributions include

- the introduction of convexity as a new dimension in human-machine alignment.
- recapitulation of salient properties of convex sets in flat and curved spaces.
- proofs that convexity is stable to relevant latent space re-parametrization.
- an efficient workflow to measure convexity in flat and curved latent spaces.
- evidence of pervasive convexity of conceptual regions in self-supervised models for images, audio, movement, text, and brain images.
- evidence that convexity of a conceptual region in a pretrained model predicts labelling accuracy following fine-tuning, see Figure 1 .

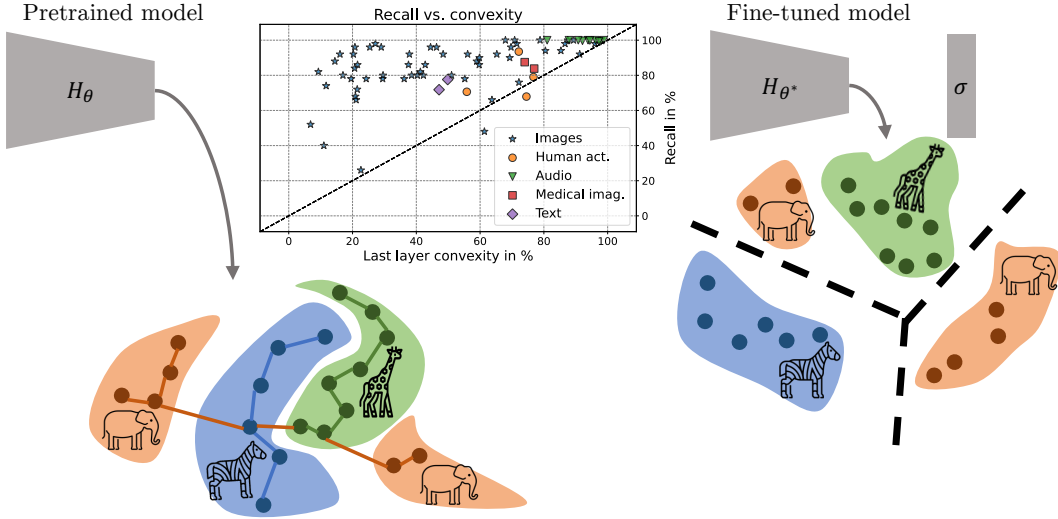


Figure 1: We measure the graph convexity of each class in the pretrained model and evaluate the recall of each class after fine-tuning. H_θ is the pretrained model, H_{θ^*} is the fine-tuned model, and σ is the classification head trained during fine-tuning. Fine-tuning involves all layers of the encoder. We present evidence (the inset and Figure 5) that higher convexity of downstream classes in the pretrained model is indicative of higher recall in the fine-tuned model.

1.2 Properties of convex sets

Let us first formalize classical convexity in Euclidean spaces.

Definition 1 (Euclidean Convexity). A subset $S \subset \mathbb{R}^D$ is convex iff $\forall \mathbf{x}, \mathbf{y} \in S \forall t \in [0, 1], \mathbf{z}(t) = t\mathbf{x} + (1-t)\mathbf{y}$ is also in S [14].

From the definition, it follows that the intersection of two convex sets is also a convex set [14]. Hence, conceptual *conjunction* (‘AND’ operation) induces convexity. *Disjunction* (‘OR’ operation), however, does not, since the union of convex sets is not necessarily convex (it is trivial to construct such examples) [14]. Euclidean convexity is conserved under affine transformations, hence convexity is robust to re-parametrization in deep networks (see proof in appendix A). Euclidean convexity is closely related to conjunctions of linear classifiers. In fact, a convex set can alternatively be defined as the intersection of linear half-spaces (possibly infinite), e.g., implemented by a set of linear decision functions resulting in a polyhedron [14].

The relevant geometric structure of deep networks is not necessarily Euclidean, hence we need to generalize to manifolds. In a Riemannian manifold M with metric tensor g , the length L of a continuously differentiable curve $\mathbf{z} : [0, 1] \rightarrow M$ is defined by $L(\mathbf{z}) = \int_0^1 \sqrt{g_{\mathbf{z}(t)}(\dot{\mathbf{z}}(t), \dot{\mathbf{z}}(t))} dt$, where $\dot{\mathbf{z}}(t) := \frac{\partial}{\partial t} \mathbf{z}(t)$. A geodesic is then a curve connecting $\mathbf{z}(0) = \mathbf{x}$ and $\mathbf{z}(1) = \mathbf{y}$, minimizing this length, i.e. $\text{geodesic}(\mathbf{x}, \mathbf{y}) = \text{argmin}_{\mathbf{z}} L(\mathbf{z})$. While geodesics are unique for Euclidean spaces, they may not be unique in manifolds. We can now generalize to geodesic convexity in manifolds:

Definition 2 (Geodesic Convexity). A region $S \in M$ is geodesic convex, iff $\forall \mathbf{x}, \mathbf{y} \in S$, there exists at least one geodesic $\mathbf{z}(t)$ connecting \mathbf{x} and \mathbf{y} , that is entirely contained in S .

When modelling latent spaces with sampled data, we must further transform the above definitions to data-driven estimators, such efforts are reported, e.g., in [40, 1]. In this paper, we choose a simple approach based on graph convexity, that applies to both Euclidean and Riemannian spaces: A subset of nodes S in a graph is convex if for all nodes in S the shortest path connecting each pair of nodes is entirely within S . Graph convexity has for instance been used to describe complex networks [47]. For sampled data, we can form a graph from Euclidean nearest neighbors (as manifolds per definition are locally Euclidean), this approach parallels the ISOMAP procedure.

We note two important properties of this estimator, first, the graph-based approximate convexity measure is invariant to isometric transformation and uniform scaling, and second, the sample-based

estimator of convexity is consistent. Both aspects are discussed further in the appendix A. The invariance to isometry and uniform scaling means that the approximate convexity property is robust to certain network re-parametrization [42].

As we will measure convexity in concept sub-graphs within larger background graphs, Dijkstra’s algorithm is preferred over ISOMAP’s Floyd–Warshall algorithm. Dijkstra’s algorithm finds the shortest path from a given node to each of the other N nodes in the graph with E edges in $\mathcal{O}(N \log N + E)$ [26, 29], while Floyd-Warshall efficiently finds the shortest distance between all vertices in the graph in $\mathcal{O}(N^3)$ [20, 28]. Since we have a sparse graph with $E \ll N^2$, Dijkstra’s algorithm will be more efficient. With these approximations, we are in a position to create a graph-based workflow for quantifying convexity in Euclidean and manifold-based structures. Note, for sampled data, we expect a certain level of noise, hence, convexity will be graded.

1.3 Neural networks and convexity

Should we expect convexity of ‘categorical’ regions in neural networks? Indeed, there are several mechanisms that could contribute to promoting convexity. First, the ubiquitous softmax is essentially a convexity-inducing device, hence, typical classification heads will induce convexity in the immediate representation. This is most easily seen by noting that softmax decision regions (maximum posterior decisions) are identical to the decision regions of a linear model, and linear models implement convex decision regions (see appendix A for formal proof). Secondly, several of the models we investigate in the present study are based on transformer architectures with attention heads. These heads contain softmax functions and are thus inducing convexity in their weighing of attention. Thirdly, typical individual artificial neurons are latent half-space detectors, and half-spaces are convex as noted above. Note that multi-layer perceptrons can approximate any non-convex decision region, including disconnected decision regions [12].

1.4 Concept based explainability

Linear-classifier-based probes are widely used in natural language processing to understand the presence of concepts in latent spaces [9, 41]. A prominent example of probe-based explanation in image classification is the TCAV scheme proposed by Kim et al. [42], in which auxiliary labelled data sets are used to identify concept directions with linear classifiers (concept class versus random images). Regions defined by linear classifiers are convex, but more general convexity is possible, c.f. above, regions defined by the intersection of a number of linear classifiers (possibly infinite). More general regional concept analysis is discussed in [21]. Following [35], three aspects are of particular importance for concept-based explainability: i) *Meaningfulness* - an explanatory concept is semantically meaningful on its own. Meaningfulness is social, i.e., individuals should associate similar meanings to the concept; ii) *Coherence* - the examples of a concept should be perceptually similar and different from examples of other concepts; iii) *Importance* - a concept is “important” for the prediction of a class if its presence is necessary ... the object whose presence is being predicted is necessary while the background is not. In our analyses, we will consider these aspects when we discuss the relevance of convex concept regions.

2 Methods

2.1 Convexity measurement workflow

We are interested in measuring the approximate convexity of a conceptual region, here, a subset of nodes in a graph. A conceptual region is a set of annotated points. Annotations can be related to *class labels*, i.e., targets for fine-tuning or *concepts*, i.e., entities that can be used for a conceptual explanation but are not directly used as targets in fine-tuning. We note that a concept can be evidence for some class labels and counter-evidence for other classes.

We first create a graph that contains all the data points of interest (comprising a region of interest and a background of data points of other classes/concepts and unannotated data). The points are nodes in the graph and the Euclidean distances between the nodes are the weights of the edges. To handle manifold-based representation, for each node, we create an undirected edge only to the nearest neighbors ($K = 10$). This procedure creates a sparse undirected weighted graph with positive weights only.

We now sample pairs of points within the given concept/class label and compute the shortest path in the graph between the pairs using Dijkstra’s algorithm [26]. For each path, we compute a score between 0 and 1. The path score is defined as the proportion of nodes on the shortest path, without the endpoints, inside the concept. If an edge directly connects the pair of nodes, the score is 1. If the points are not connected, the score is 0. We average the scores for all paths and all concepts/classes and get one number for concepts and one for classes per layer. Error bars in the results show the standard error of the mean, where we set n to the number of points in the given concept/class. This is likely a conservative estimate since the mean is based on much more pairs than there are points. The score depends on the number of concepts and classes, and also on the number of data points per class/concept. It follows that our results are not directly comparable across modalities. To mitigate this problem, we balance the class and concept data and add background points not belonging to any class or concept.

Measurements based on neighbors in high dimensional data can be sensitive to the so-called hubness problem [51]. We evaluate the hubness of the latent representations in terms of k-skewness and the Robinhood score. Results are deferred to the appendix C.1-C.5, since only mild hubness issues were detected for most domains. We decided to analyse convexity without adjustment for hubness, to avoid possible biases introduced by normalization schemes [51].

2.2 Domains and data

Image domain. We used the ImageNet-1k images and class labels [53, 24] in our experiments. The validation set contains 50 images per class. We used additional *concepts* of two types: texture and colors. Texture data comes from Describable Textures Dataset (DTD) [19]. It contains 47 textures with 120 images per texture. Color data is a combination of images from [2] and Digikala Products Color Classification.¹ We have 9 colors and for each color, we used all images from the Color classification dataset and supplied them with randomly sampled images of the corresponding color from Digikala. For this experiment, we balanced the number of concepts and classes and the number of image examples in each. We randomly chose 56 ImageNet classes and 50 images from each concept. In total, we have 2800 "concept" images and 2800 "class" images. To simulate random background images, we added 5600 images from the validation set of Places365 [44].

The network model is data2vec-base [3]. For details on architecture and training, see appendix B.1. We extracted the input embedding together with 12 layers of dimension 768 for geometric analysis.

Human activity domain. We used a pretrained human activity model from [67] to extract the latent representations. The model is pretrained in a self-supervised manner on a large unlabelled dataset from the UK Biobank. The model follows the architecture of ResNet-V2 with 1D convolutions and a total of 21 convolutional layers. The resulting feature vector after the final pretrained layer is of dimension 1024. For additional information on the network and the data see appendix B.2. For testing the convexity of the model, we use the Capture24 dataset [65]. In [62], the original set of 213 labels was divided into 4 coarse class labels, namely: sleeping, sedentary behavior, light physical activity behaviors, and moderate-to-vigorous physical activity behaviors based on the metabolic equivalent of task (MET) scores. These 4 labels are used as classes when fine-tuning the model. In [65] the MET score is similarly used to divide the labels into 11 categories. One of the categories overlaps with the 'sleep' label from the classes and is thus excluded. The remaining 10 categories are used as human activity *concepts*. Since all data points are associated with both a label and a concept, the convexity analysis is done separately for classes and concepts. For each concept, we sample 1000 points (or the maximum number available), we then sample 1000 points (or maximum available) from each of the remaining concepts (as well as the class label 'sleep') to use as background. This yields a total of $N = 9139$ points. We sample N points from the WISDM human activity dataset [64] to add as background points. We then analyze the convexity of each concept. We subsequently map all points to their corresponding class and analyze the convexity of each class on the same graph.

Audio domain. We use the pretrained wav2vec2.0 model [4], pretrained on the Librispeech corpus (960h of unlabeled data) [49]. The model consists of a CNN-based feature encoder, a transformer-based context network, and a quantization module. We are especially interested in the latent space representation in the initial embedding layer and the 12 transformer layers. After each layer, we extract the feature vector of dimension 768.

¹<https://www.kaggle.com/datasets/masouduut94/digikala-color-classification>

We fine-tuned the model to perform digit classification based on the AudioMNIST dataset [8], which consists of 30000 audio recordings of spoken digits (0-9) in English of 60 different speakers (with 50 repetitions per digit). For additional information see the appendix B.3. For the convexity analysis, we compare the latent representations of different classes and concepts. For the AudioMNIST dataset, the classes are the 10 digits. As concepts we use gender and speaker id, which are provided as metadata of the dataset. Additionally, we transcribe the phonemes of each audio file using "WebMAUS Basic" [56]. The phonemes of each audio file are cut into individual audio files and the latent representations are extracted for each phoneme. To evaluate the robustness of the results, relevant background points are added to the dataset, that do not overlap with the classes. In the audio case, the Speech Commands dataset [8] was used to provide these background points. Ten words ('yes', 'no', 'up', 'down', 'left', 'right', 'on', 'off', 'stop', 'go') with 600 repetitions each (matching the data amount of the test set) were randomly chosen from the dataset.

Text domain. Our NLP case study is the base version of RoBERTa [43], which is pretrained to perform Masked Language Modelling [25] in order to reconstruct masked pieces of text. The model consists of an embedding layer followed by 12 transformer encoder layers. The pretraining of RoBERTa was performed on 160GB of uncompressed English-language text in order to learn latent representations of text which are expressed as 768-dimensional vectors.

Fine-tuning class labels were the simple positive or negative sentiment annotations of the TweetEval dataset [6, 52]. The GoEmotions dataset [23] is used to provide related concepts. The dataset is a filtered collection of texts from `reddit.com` which are labelled in accordance with the emotions they express. There is a total of 27 different categories of emotions which are labelled in the dataset. Texts can be annotated with multiple labels and are labelled multiple times by different annotators. In order to have a simple text-label relationship we only consider a single random instance of an annotation of each text and a single label that will define the text's concept. In order to balance and minimize the dataset, we only consider a subset of 12 emotions with an even split between emotions that are associated with positive and negative sentiment. Of this subset, we sample 300 texts from each of the 12 emotions. Additionally, we also include 300 "neutral" texts, which are also labelled in the GoEmotions dataset, to act as background data points for some experiments. All data were obtained from HuggingFace. For additional details see appendix B.4.

Medical Imaging domain. Anatomically (T1) weighted 3T Magnetic Resonance Imaging (MRI) data with gender labels are obtained from the Human Connectome Project S1200 Subjects Release [60]. We use the structurally preprocessed data as described in [36] of 1113 subjects. We train a self-supervised model using a modified version of the Masked-Auto-Encoder (MAE) [38], for details see appendix B.5. We use anatomical brain regions as concepts and gender as class labels (for fine-tuning). To define brain regions, the original segmentation mask consisting of multiple cortical and sub-cortical regions is downsampled to 13 distinct major regions: White Matter, Ventricles, Cerebellum, Thalamus, Caudate, Putamen, Pallidum, Brain-Stem, Hippocampus, Amygdala, Accumbens, Corpus, Callosum and Cortex. To obtain the feature vector \mathbf{v} for a particular concept c in layer l , we calculate the weighted sum over all embedding vectors \mathbf{u}_j over the subvolume j , such that $v_{l,c} = \sum_{j=1}^J w_{c,j} \mathbf{u}_{l,j}$, where $w_{c,j}$ is the ratio of voxels labelled with concept c in subvolume j and the total number of voxels in j and $\sum_{j=1}^J w_{c,j} = 1$. To retrieve the feature vector \mathbf{v}_l for the class label gender in layer l , we calculate the mean over all subvolumes, i.e. $w = \frac{1}{J}$. For a total of B subjects, this results in $B \cdot (13 + 2)$ feature vectors for 13 concepts and 2 classes. For the convexity analysis, we sample 200 subjects for each class and concept as well as 200 subjects used as background points, none of which were used in the training set for pretraining or fine-tuning.

3 Results

3.1 Structure of latent representations of the image domain before and after fine-tuning

To gain intuition on the effect of fine-tuning, we first inspect t-SNE plots for a subset of classes and concepts (Figure 11) of the image domain. Interestingly, while the pretrained model never 'saw' the labels, it clusters both the classes and concepts towards the end of the network. The *background* points are well mixed with both concepts and classes, presenting evidence that they are in scope for the network although they originate from a completely different source. The observed structure in

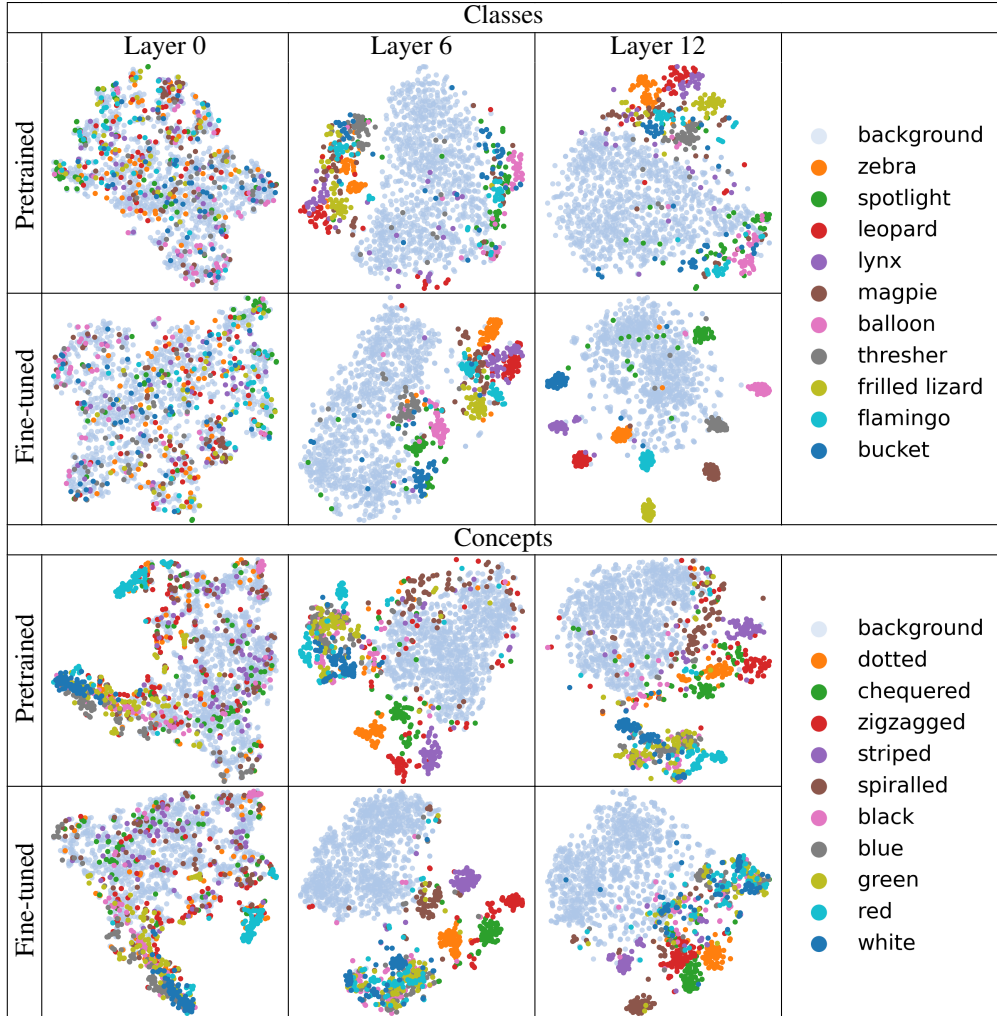


Figure 2: Images: t-SNE plots for a subset of classes (top) and concepts (bottom), with 50 images per concept or class and 1000 background points, both before and after fine-tuning.

these low-dimensional representations adds motivation to our investigation of the convexity of both class labels and concept regions in the high dimensional latent spaces.

After fine-tuning, we find, as expected, that the model representation clearly separates the classes in the last layer. Figure 11 shows that color concepts are mostly clustered in the input layer, whereas texture concepts get more clustered towards the end of the model.

The left panel in Figure 3 shows the convexity scores across all layers for the image domain and the right panel for the audio domain. For images, we notice that the convexity of classes increases throughout the network. The convexity of concepts initially increases but decreases in the second half of the model. Similar results are obtained when the analysis does not include background points (details in appendix C.1). The scores for both concepts and classes increase after fine-tuning for the image domain. For the audio data, the figure shows that the concepts phonemes and speaker ID react different to the fine-tuning. Phonemes, being relevant for recognition increase their convexity upon fine-tuning, while the irrelevant speaker ID decreases in convexity as expected.

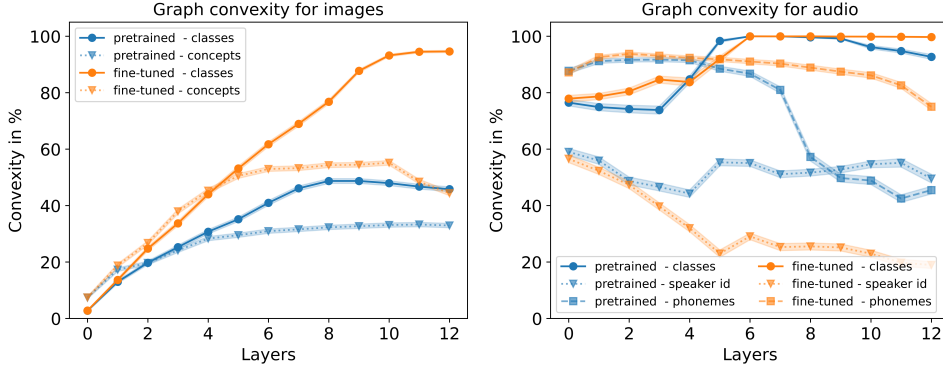


Figure 3: Graph convexity scores for images (left) and audio (right). The light color bands show the standard error of the mean as discussed in Section 2.1. The image results were computed on 56 classes + 56 concepts (50 images per concept/class) + 5600 background points. The audio results were computed on 10 classes, 12 speaker ids and 20 phonemes + 6000 background points.

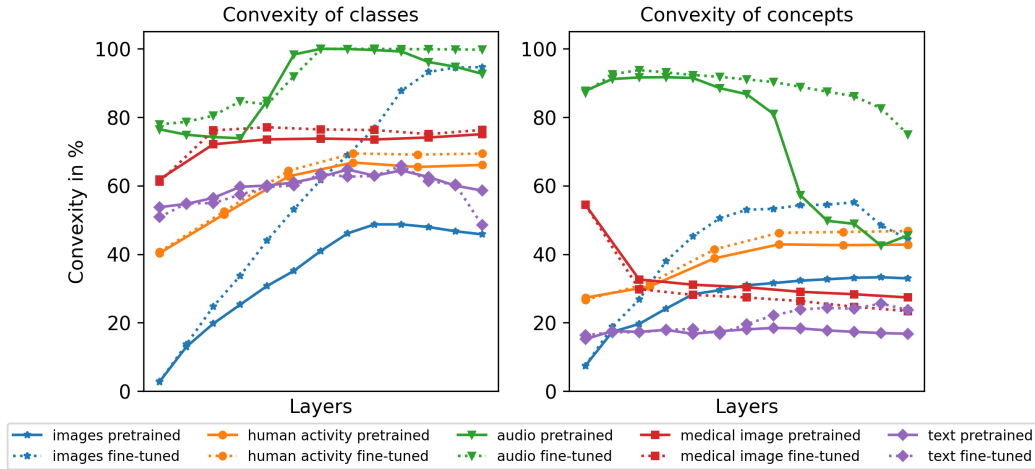


Figure 4: Graph convexity scores for all modalities. Convexity is pervasive in all networks. The number of layers differs across models but the most-left layer is the first layer that we observe and the right-most layer is the last layer in each model. For audio, the concept phonemes is displayed. Error bars are omitted in this plot for clarity (see the figures of individual modalities in the appendices C.1-C.5). Note that the results are not directly comparable across modalities (see Section 2.1).

3.2 Cross domain analysis

We measure convexity for classes and concepts within the pre-trained networks and after fine-tuning with class labels as targets. Figure 4 shows the results for all modalities. The convexity is pervasive both before and after fine-tuning. Generally, class convexity is increased by fine-tuning, however, for the concepts, the picture is more mixed. This is expected as concepts can be differentially associated with labels or a subset of labels, as we saw exemplified in the audio domain.

For detailed results of the analysis of individual data modalities, see appendix C.1-C.5.

To test the cognitive science motivated hypothesis that convexity facilitates categorization, we plot the post-fine-tuning accuracy (recall) as a function of pretraining convexity in Figure 5. The link is non-linear but there is a pronounced relation so that high convexity in the pre-trained model predicts high accuracy after fine-tuning. The link is stronger the more data enters the fine-tuning.

Ghorbani et al. [35] listed core dimensions for our understanding of concept-based understanding of machine-learned representations. We find that these dimensions are well aligned with both the relevant cognitive science foundation of our investigation and with the new results. *Meaningfulness*,

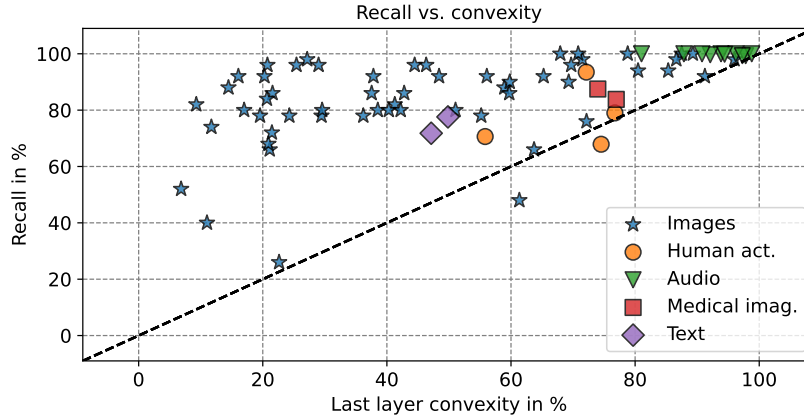


Figure 5: Convexity of a subset of classes in the pretrained models vs. recall of these classes in the fine-tuned models for all data domains. The standard errors of the mean for the graph convexity scores are on average (for images, human activity, audio, text, and brain, respectively) 0.85, 0.33, 0.11, 3.06, 2.36, and the standard errors of the mean for the accuracy are on average 4.55, 0.82, 0.31, 1.37, 3.36 (see appendix C for the plot with included error bars). The correlation coefficient is 0.52.

i.e., an explanatory concept is semantically meaningful on its own. We note that such construction of meaning is social, i.e., individuals should associate similar meanings to the concept. This is related to the notion of *naturalness* of concepts in cognitive science. Convexity of category regions in human and machine representations is consistent with the concept of *coherence*, i.e., examples of a concept should be perceptually similar, and different from examples of other concepts. Finally, the *importance* of a category label can be linked to objectives such as downstream fine-tuning accuracy. We found that pretraining label region convexity predicts subsequent generalization following fine-tuning indicating that *convexity could be an importance signal for categorization*.

4 Conclusion

Understanding machine and human representational spaces is important for alignment and trust. Such investigations can be furthered by aligning the vocabularies of investigations into human and machine representations. Inspired by the conceptual spaces research of Gärdenfors and coworkers, we introduce the idea of convexity as a new dimension in human-machine alignment. Convexity is closely related to generalization in cognitive systems. Machine representations can be best described by curved spaces, hence, we recapitulated salient properties of convex sets in flat and curved spaces. We found that convexity is stable to relevant latent space re-parametrizations for deep networks. We developed a workflow for the estimation of approximate convexity based on graph methods which can be used to measure convexity in flat and curved latent spaces. We carried out extensive experiments in multiple domains including visual object recognition, human activity data, audio, text, and medical imaging. Our experiments included networks trained by self-supervised learning and next fine-tuned on domain-specific labels. We found evidence of pervasive convexity of conceptual regions in pretrained models. On fine-tuning, we found that class region convexity generally increases, while for other (untrained) concepts, convexity may increase or decrease reflecting such concepts' relevance to labels. Importantly, we found evidence across the data domains that label region convexity in the pretrained networks predict accuracy following fine-tuning. Remind, the pretrained networks have not 'seen' the labels. The latter observation is evidence that the convexity signal is an indicator of how well pretrained networks are prepared for future generalizations by the self-supervised learning procedure.

5 Limitations and broader impact

Limitations: Our graph convexity workflow is quite general. However, it is limited by uncertainty related to the number of sampled points, the number of concepts and classes, etc. Although we

evaluate convexity in several modalities, there are fundamental limitations when directly comparing results across modalities because of the differences in data, label structures, and models available.

Broader impact: Human-machine alignment is important for human-centered AI. The development of common vocabularies and representational analyses can support the understanding of alignment. The field of explainable AI has developed a plethora of methods to better understand black-box models and avoid undesirable biases. It is an aim of the present work to contribute towards this goal. We acknowledge that such understanding can also be used by adversaries and increase the risk of misuse.

Acknowledgments and Disclosure of Funding

This work was supported by the DIREC Bridge project Deep Learning and Automation of Imaging-Based Quality of Seeds and Grains, Innovation Fund Denmark grant number 9142-00001B. This work was supported by the Pioneer Centre for AI, DNRF grant number P1 and the Novo Nordisk Foundation grant NNF22OC0076907 "Cognitive spaces - Next generation explainability". This work was supported by the Danish Data Science Academy, which is funded by the Novo Nordisk Foundation (NNF21SA0069429) and VILLUM FONDEN (40516). This work was partially supported by DeiC National HPC (g.a. DeiC-DTU-N5-20230028) and by the "Alignment of human and machine representations" project (g.a. DeiC-DTU-N5-20230033) and by the "self-supervised brain model" project (g.a. DeiC-DTU-S5-202300105). We acknowledge Danish e-infrastructure Cooperation (DeiC), Denmark, for awarding this project access to the LUMI supercomputer, owned by the EuroHPC Joint Undertaking, hosted by CSC (Finland) and the LUMI consortium through Danish e-infrastructure Cooperation (DeiC), Denmark, "Alignment of human and machine representations", DeiC-DTU-N5-20230028.

References

- [1] G. Arvanitidis, L. K. Hansen, and S. Hauberg. Latent space oddity: on the curvature of deep generative models. In *6th International Conference on Learning Representations, ICLR 2018, Vancouver, BC, Canada, April 30 - May 3, 2018, Conference Track Proceedings*. OpenReview.net, 2018.
- [2] A. Ayanzadeh. Color classification, 2018.
- [3] A. Baevski, W.-N. Hsu, Q. Xu, A. Babu, J. Gu, and M. Auli. Data2vec: A general framework for self-supervised learning in speech, vision and language. In *International Conference on Machine Learning*, pages 1298–1312. PMLR, 2022.
- [4] A. Baevski, Y. Zhou, A. Mohamed, and M. Auli. wav2vec 2.0: A framework for self-supervised learning of speech representations. *Advances in neural information processing systems*, 33:12449–12460, 2020.
- [5] C. Balkenius and P. Gärdenfors. Spaces in the brain: From neurons to meanings. *Frontiers in psychology*, 7:1820, 2016.
- [6] F. Barbieri, J. Camacho-Collados, L. Espinosa-Anke, and L. Neves. TweetEval: Unified Benchmark and Comparative Evaluation for Tweet Classification. In *Proceedings of Findings of EMNLP*, 2020.
- [7] L. Bechberger and K.-U. Kühnberger. Grounding psychological shape space in convolutional neural networks. In *Software Engineering and Formal Methods. SEFM 2021 Collocated Workshops: CIFMA, CoSim-CPS, OpenCERT, ASYDE, Virtual Event, December 6–10, 2021, Revised Selected Papers*, pages 86–106. Springer, 2022.
- [8] S. Becker, M. Ackermann, S. Lapuschkin, K.-R. Müller, and W. Samek. Interpreting and explaining deep neural networks for classification of audio signals. *arXiv preprint arXiv:1807.03418*, 2018.
- [9] Y. Belinkov, N. Durrani, F. Dalvi, H. Sajjad, and J. Glass. What do neural machine translation models learn about morphology? In *Proceedings of the 55th Annual Meeting of the Association for Computational Linguistics (Volume 1: Long Papers)*, pages 861–872, 2017.

- [10] E. M. Bender, T. Gebru, A. McMillan-Major, and S. Shmitchell. On the dangers of stochastic parrots: Can language models be too big? In *Proceedings of the 2021 ACM conference on fairness, accountability, and transparency*, pages 610–623, 2021.
- [11] M. Bernstein, V. De Silva, J. C. Langford, and J. B. Tenenbaum. Graph approximations to geodesics on embedded manifolds. Technical report, Citeseer, 2000.
- [12] C. M. Bishop et al. *Neural networks for pattern recognition*. Oxford university press, 1995.
- [13] C. M. Bishop and N. M. Nasrabadi. *Pattern recognition and machine learning*. Springer, 2006.
- [14] S. P. Boyd and L. Vandenberghe. *Convex Optimization*. Cambridge University Press, 2004.
- [15] P. P. Brahma, D. Wu, and Y. She. Why deep learning works: A manifold disentanglement perspective. *IEEE transactions on neural networks and learning systems*, 27(10):1997–2008, 2015.
- [16] M. J. Cardoso, W. Li, R. Brown, N. Ma, E. Kerfoot, Y. Wang, B. Murray, A. Myronenko, C. Zhao, D. Yang, V. Nath, Y. He, Z. Xu, A. Hatamizadeh, W. Zhu, Y. Liu, M. Zheng, Y. Tang, I. Yang, M. Zephyr, B. Hashemian, S. Alle, M. Zalbagi Darestani, C. Budd, M. Modat, T. Vercauteren, G. Wang, Y. Li, Y. Hu, Y. Fu, B. Gorman, H. Johnson, B. Genereaux, B. S. Erdal, V. Gupta, A. Diaz-Pinto, A. Dourson, L. Maier-Hein, P. F. Jaeger, M. Baumgartner, J. Kalpathy-Cramer, M. Flores, J. Kirby, L. A. Cooper, H. R. Roth, D. Xu, D. Bericat, R. Floca, S. K. Zhou, H. Shuaib, K. Farahani, K. H. Maier-Hein, S. Aylward, P. Dogra, S. Ourselin, and A. Feng. MONAI: An open-source framework for deep learning in healthcare. Nov. 2022.
- [17] B. Christian. *The alignment problem: Machine learning and human values*. WW Norton & Company, 2020.
- [18] S. Chung and L. Abbott. Neural population geometry: An approach for understanding biological and artificial neural networks. *Current opinion in neurobiology*, 70:137–144, 2021.
- [19] M. Cimpoi, S. Maji, I. Kokkinos, S. Mohamed, and A. Vedaldi. Describing textures in the wild. In *Proceedings of the IEEE Conf. on Computer Vision and Pattern Recognition (CVPR)*, 2014.
- [20] T. H. Cormen, C. E. Leiserson, R. L. Rivest, and C. Stein. *Introduction to Algorithms, 4th edition*. MIT press, 2022.
- [21] J. Crabbé and M. van der Schaar. Concept activation regions: A generalized framework for concept-based explanations. In *NeurIPS*, 2022.
- [22] E. Davis and S. Sethuraman. Approximating geodesics via random points. *The Annals of Applied Probability*, 29(3):1446–1486, 2019.
- [23] D. Demszky, D. Movshovitz-Attias, J. Ko, A. Cowen, G. Nemade, and S. Ravi. Goemotions: A dataset of fine-grained emotions. *arXiv preprint arXiv:2005.00547*, 2020.
- [24] J. Deng, W. Dong, R. Socher, L.-J. Li, K. Li, and L. Fei-Fei. ImageNet: A Large-Scale Hierarchical Image Database. In *CVPR09*, 2009.
- [25] J. Devlin, M.-W. Chang, K. Lee, and K. Toutanova. Bert: Pre-training of deep bidirectional transformers for language understanding. *arXiv preprint arXiv:1810.04805*, 2018.
- [26] E. W. Dijkstra. A note on two problems in connexion with graphs. *Numerische Mathematik*, 1:269–271, 1959.
- [27] I. Douven, S. Elqayam, P. Gärdenfors, and P. Mirabile. Conceptual spaces and the strength of similarity-based arguments. *Cognition*, 218:104951, 2022.
- [28] R. W. Floyd. Algorithm 97: Shortest path. *Commun. ACM*, 5(6):345, 1962.
- [29] M. L. Fredman and R. E. Tarjan. Fibonacci heaps and their uses in improved network optimization algorithms. *J. ACM*, 34(3):596–615, 1987.
- [30] P. Gärdenfors. Induction, conceptual spaces and ai. *Philosophy of Science*, 57(1):78–95, 1990.
- [31] P. Gärdenfors. Concept learning: a geometrical model. In *Proceedings of the Aristotelian Society (Hardback)*, volume 101, pages 163–183. Wiley Online Library, 2001.
- [32] P. Gardenfors. *The geometry of meaning: Semantics based on conceptual spaces*. MIT press, 2014.
- [33] P. Gärdenfors, J. Jost, and M. Warglien. From actions to effects: Three constraints on event mappings. *Frontiers in psychology*, 9:1391, 2018.

- [34] P. Gärdenfors and M.-A. Williams. Reasoning about categories in conceptual spaces. In *IJCAI*, pages 385–392, 2001.
- [35] A. Ghorbani, J. Wexler, J. Y. Zou, and B. Kim. Towards automatic concept-based explanations. *Advances in Neural Information Processing Systems*, 32, 2019.
- [36] M. F. Glasser, S. N. Sotiropoulos, J. A. Wilson, T. S. Coalson, B. Fischl, J. L. Andersson, J. Xu, S. Jbabdi, M. Webster, J. R. Polimeni, D. C. Van Essen, and M. Jenkinson. The minimal preprocessing pipelines for the human connectome project. *NeuroImage*, 80:105–124, 2013. Mapping the Connectome.
- [37] A. Goldstein, Z. Zada, E. Buchnik, M. Schain, A. Price, B. Aubrey, S. A. Nastase, A. Feder, D. Emanuel, A. Cohen, et al. Shared computational principles for language processing in humans and deep language models. *Nature neuroscience*, 25(3):369–380, 2022.
- [38] K. He, X. Chen, S. Xie, Y. Li, P. Dollár, and R. Girshick. Masked autoencoders are scalable vision learners. In *Proceedings of the IEEE/CVF Conference on Computer Vision and Pattern Recognition (CVPR)*, pages 16000–16009, June 2022.
- [39] O. J. Hénaff, R. L. Goris, and E. P. Simoncelli. Perceptual straightening of natural videos. *Nature neuroscience*, 22(6):984–991, 2019.
- [40] O. J. Hénaff and E. P. Simoncelli. Geodesics of learned representations. In Y. Bengio and Y. LeCun, editors, *4th International Conference on Learning Representations, ICLR 2016, San Juan, Puerto Rico, May 2-4, 2016, Conference Track Proceedings*, 2016.
- [41] J. Hewitt and P. Liang. Designing and interpreting probes with control tasks. In *Proceedings of the 2019 Conference on Empirical Methods in Natural Language Processing and the 9th International Joint Conference on Natural Language Processing (EMNLP-IJCNLP)*, pages 2733–2743, 2019.
- [42] B. Kim, M. Wattenberg, J. Gilmer, C. Cai, J. Wexler, F. Viegas, et al. Interpretability beyond feature attribution: Quantitative testing with concept activation vectors (tcav). In *International conference on machine learning*, pages 2668–2677. PMLR, 2018.
- [43] Y. Liu, M. Ott, N. Goyal, J. Du, M. Joshi, D. Chen, O. Levy, M. Lewis, L. Zettlemoyer, and V. Stoyanov. Roberta: A robustly optimized bert pretraining approach. *arXiv preprint arXiv:1907.11692*, 2019.
- [44] A. López-Cifuentes, M. Escudero-Vinolo, J. Bescós, and Á. García-Martín. Semantic-aware scene recognition. *Pattern Recognition*, 102:107256, 2020.
- [45] K. Mahowald, A. A. Ivanova, I. A. Blank, N. Kanwisher, J. B. Tenenbaum, and E. Fedorenko. Dissociating language and thought in large language models: a cognitive perspective. *arXiv preprint arXiv:2301.06627*, 2023.
- [46] J. Mamou, H. Le, M. Del Rio, C. Stephenson, H. Tang, Y. Kim, and S. Chung. Emergence of separable manifolds in deep language representations. *arXiv preprint arXiv:2006.01095*, 2020.
- [47] T. Marc and L. Šubelj. Convexity in complex networks. *Network Science*, 6(2):176–203, 2018.
- [48] S. Mika, B. Schölkopf, A. Smola, K.-R. Müller, M. Scholz, and G. Rätsch. Kernel pca and de-noising in feature spaces. *Advances in neural information processing systems*, 11, 1998.
- [49] V. Panayotov, G. Chen, D. Povey, and S. Khudanpur. Librispeech: an asr corpus based on public domain audio books. In *2015 IEEE international conference on acoustics, speech and signal processing (ICASSP)*, pages 5206–5210. IEEE, 2015.
- [50] G. Parascandolo, N. Kilbertus, M. Rojas-Carulla, and B. Schölkopf. Learning independent causal mechanisms. In *International Conference on Machine Learning*, pages 4036–4044. PMLR, 2018.
- [51] M. Radovanović, A. Nanopoulos, and M. Ivanović. Hubs in space: Popular nearest neighbors in high-dimensional data. *The Journal of Machine Learning Research*, 11:2487–2531, 2010.
- [52] S. Rosenthal, N. Farra, and P. Nakov. Semeval-2017 task 4: Sentiment analysis in twitter. In *Proceedings of the 11th international workshop on semantic evaluation (SemEval-2017)*, pages 502–518, 2017.
- [53] O. Russakovsky, J. Deng, H. Su, J. Krause, S. Satheesh, S. Ma, Z. Huang, A. Karpathy, A. Khosla, M. Bernstein, A. C. Berg, and L. Fei-Fei. ImageNet Large Scale Visual Recognition Challenge. *International Journal of Computer Vision (IJCV)*, 115(3):211–252, 2015.

- [54] R. N. Shepard. Toward a universal law of generalization for psychological science. *Science*, 237(4820):1317–1323, 1987.
- [55] C. Ströbner. Criteria for naturalness in conceptual spaces. *Synthese*, 200(2):78, 2022.
- [56] J. Strunk, F. Schiel, F. Seifart, et al. Untrained forced alignment of transcriptions and audio for language documentation corpora using webmaus. In *LREC*, pages 3940–3947, 2014.
- [57] J. Tang, A. LeBel, S. Jain, and A. G. Huth. Semantic reconstruction of continuous language from non-invasive brain recordings. *Nature Neuroscience*, pages 1–9, 2023.
- [58] J. B. Tenenbaum, V. d. Silva, and J. C. Langford. A global geometric framework for nonlinear dimensionality reduction. *science*, 290(5500):2319–2323, 2000.
- [59] L. Valeriani, D. Doimo, F. Cuturello, A. Laio, A. Ansuini, and A. Cazzaniga. The geometry of hidden representations of large transformer models. *arXiv preprint arXiv:2302.00294*, 2023.
- [60] D. C. Van Essen, S. M. Smith, D. M. Barch, T. E. Behrens, E. Yacoub, and K. Ugurbil. The wu-minn human connectome project: An overview. *NeuroImage*, 80:62–79, 2013. Mapping the Connectome.
- [61] A. Vaswani, N. Shazeer, N. Parmar, J. Uszkoreit, L. Jones, A. N. Gomez, Ł. Kaiser, and I. Polosukhin. Attention is all you need. *Advances in neural information processing systems*, 30, 2017.
- [62] R. Walmsley, S. Chan, K. Smith-Byrne, R. Ramakrishnan, M. Woodward, K. Rahimi, T. Dwyer, D. Bennett, and A. Doherty. Reallocation of time between device-measured movement behaviours and risk of incident cardiovascular disease. *British Journal of Sports Medicine*, 56(18):1008–1017, 2022.
- [63] M. Warglien and P. Gärdenfors. Semantics, conceptual spaces, and the meeting of minds. *Synthese*, 190(12):2165–2193, Aug 2013.
- [64] G. M. Weiss, K. Yoneda, and T. Hayajneh. Smartphone and smartwatch-based biometrics using activities of daily living. *IEEE Access*, 7:133190–133202, 2019.
- [65] M. Willetts, S. Hollowell, L. Aslett, C. Holmes, and A. Doherty. Statistical machine learning of sleep and physical activity phenotypes from sensor data in 96,220 UK biobank participants. *Sci. Rep.*, 8(1):7961, May 2018.
- [66] T. Wolf, L. Debut, V. Sanh, J. Chaumond, C. Delangue, A. Moi, P. Cistac, T. Rault, R. Louf, M. Funtowicz, J. Davison, S. Shleifer, P. von Platen, C. Ma, Y. Jernite, J. Plu, C. Xu, T. L. Scao, S. Gugger, M. Drame, Q. Lhoest, and A. M. Rush. Transformers: State-of-the-art natural language processing. In *Proceedings of the 2020 Conference on Empirical Methods in Natural Language Processing: System Demonstrations*, pages 38–45, Online, Oct. 2020. Association for Computational Linguistics.
- [67] H. Yuan, S. Chan, A. P. Creagh, C. Tong, D. A. Clifton, and A. Doherty. Self-supervised learning for human activity recognition using 700,000 person-days of wearable data, 2022.

Appendices

Contents

A	Theory	14
A.1	Softmax induces convexity	14
A.2	Euclidean convexity is invariant to affine transformations	15
A.3	Graph convexity is invariant to isometry and uniform scaling	15
A.4	Consistency of graph estimates of geodesics	16
B	Data sets	16
B.1	Image domain	16
B.2	Human activity domain	17
B.3	Audio domain	17
B.4	Text domain	18
B.5	Medical Imaging domain	19
C	Detailed Results	19
C.1	Image domain	19
C.2	Human activity domain	20
C.3	Audio domain results	21
C.4	Text results	21
C.5	Medical Imaging Results	22
C.6	Recall vs. convexity	28

A Theory

In this appendix we present some mathematical background and intuition for the approximate convexity workflow.

A.1 Softmax induces convexity

Theorem 1. *The preimage of each decision region under the last dense layer and softmax function is a convex set. More precisely: Let us denote the output of the last dense layer by*

$$a_k(\mathbf{z}) = \sum_{j=1}^J w_{k,j} z_j \tag{1}$$

for $\mathbf{z} \in \mathbb{R}^n$ and the probabilities

$$p_k(\mathbf{z}) = \frac{\exp a_k(\mathbf{z})}{\sum_{k'=1}^K \exp a_{k'}(\mathbf{z})}. \tag{2}$$

Denote

$$C_k \subseteq \mathbb{R}^n = \{\mathbf{x} \in \mathbb{R}^n : p_k(\mathbf{x}) > p_j(\mathbf{x}) \forall j \in \{1, \dots, K\}, j \neq k\}. \tag{3}$$

Then C_k is a convex set for any $k \in \{1, \dots, K\}$ [13].

Proof. Let us define regions

$$\mathbf{x} \in \mathcal{R}_k \iff (a_k(\mathbf{x}) > a_j(\mathbf{x}) \forall j \neq k). \tag{4}$$

Because $\sum_{k'=1}^K \exp a_{k'} > 0$ and by the monotonicity of the exponential function, it holds that

$$k_{opt}(\mathbf{x}) := \arg \max_k p_k(\mathbf{x}) = \arg \max_k \frac{\exp a_k(\mathbf{x})}{\sum_{k'=1}^K \exp a_{k'}(\mathbf{x})} = \arg \max_k a_k(\mathbf{x}), \tag{5}$$

Therefore,

$$\mathcal{R}_k = \mathcal{C}_k \quad \forall k \in \{1, \dots, K\} \quad (6)$$

and we can from now on work with \mathcal{R}_k .

Following the definitions from [13], pages 182-184:

Let $\mathbf{x}_A, \mathbf{x}_B \in \mathcal{R}_k$ and define any point $\hat{\mathbf{x}}$ that lies on the line connecting the two:

$$\hat{\mathbf{x}} = \lambda \mathbf{x}_A + (1 - \lambda) \mathbf{x}_B, \quad (7)$$

where $0 \leq \lambda \leq 1$. Cf. (1), the discriminant functions, a_k , are linear and it follows that:

$$a_k(\hat{\mathbf{x}}) = \lambda a_k(\mathbf{x}_A) + (1 - \lambda) a_k(\mathbf{x}_B) \quad (8)$$

for all k . From the definition of \mathcal{R}_k , we know that $a_k(\mathbf{x}_A) > a_j(\mathbf{x}_A)$ and $a_k(\mathbf{x}_B) > a_j(\mathbf{x}_B)$ for all $j \neq k$. Therefore, $a_k(\hat{\mathbf{x}}) > a_j(\hat{\mathbf{x}})$ for all $j \neq k$ and $\hat{\mathbf{x}}$ belongs to \mathcal{R}_k . Hence, $\mathcal{R}_k = \mathcal{C}_k$ is convex. \square

Remark. Given a classifier with high accuracy, it follows that most of the data points lie in the decision region corresponding to their correct class. In this case, the embeddings before the final linear layer belonging to the same class will be an (almost) convex set.

A.2 Euclidean convexity is invariant to affine transformations

Theorem 2. Let $f : \mathbb{R}^n \rightarrow \mathbb{R}^n$ be an affine transformation (i.e., $f(\mathbf{x}) = \mathbf{A}\mathbf{x} + \mathbf{b}$, where $\mathbf{b} \in \mathbb{R}^n$ and $\mathbf{A} : \mathbb{R}^n \rightarrow \mathbb{R}^n$ is an invertible linear transformation). Let $X \subset \mathbb{R}^n$ be a convex set. Then $f(X)$ is convex [14].

Proof. Let $\mathbf{x}, \mathbf{y} \in f(X)$ and $\lambda \in [0, 1]$. There exist $\bar{\mathbf{x}}, \bar{\mathbf{y}} \in X$ such that $f(\bar{\mathbf{x}}) = \mathbf{x}$ and $f(\bar{\mathbf{y}}) = \mathbf{y}$. Since X is convex, we have $\lambda \bar{\mathbf{x}} + (1 - \lambda) \bar{\mathbf{y}} \in X$. Therefore,

$$f(\lambda \bar{\mathbf{x}} + (1 - \lambda) \bar{\mathbf{y}}) \in f(X). \quad (9)$$

Moreover, because of the linearity of A ,

$$f(\lambda \bar{\mathbf{x}} + (1 - \lambda) \bar{\mathbf{y}}) = \mathbf{A}(\lambda \bar{\mathbf{x}} + (1 - \lambda) \bar{\mathbf{y}}) + \mathbf{b} = \lambda \mathbf{A}\bar{\mathbf{x}} + (1 - \lambda) \mathbf{A}\bar{\mathbf{y}} + \mathbf{b}. \quad (10)$$

Finally, we have

$$\lambda \mathbf{A}\bar{\mathbf{x}} + (1 - \lambda) \mathbf{A}\bar{\mathbf{y}} + \mathbf{b} = \lambda (\mathbf{A}\bar{\mathbf{x}} + \mathbf{b}) + (1 - \lambda) (\mathbf{A}\bar{\mathbf{y}} + \mathbf{b}) \quad (11)$$

$$= \lambda f(\bar{\mathbf{x}}) + (1 - \lambda) f(\bar{\mathbf{y}}) \quad (12)$$

$$= \lambda \mathbf{x} + (1 - \lambda) \mathbf{y}. \quad (13)$$

Hence,

$$f(\lambda \bar{\mathbf{x}} + (1 - \lambda) \bar{\mathbf{y}}) = \lambda \mathbf{x} + (1 - \lambda) \mathbf{y} \quad (14)$$

and $\lambda \mathbf{x} + (1 - \lambda) \mathbf{y} \in f(X)$. Therefore, $f(X)$ is convex. \square

A.3 Graph convexity is invariant to isometry and uniform scaling

Theorem 3. Graph convexity is invariant to isometry and uniform scaling.

Proof. Isometry (with respect to Euclidean distance) is a map $I : \mathbb{R}^n \rightarrow \mathbb{R}^n$ such that

$$\forall \mathbf{x}, \mathbf{y} \in \mathbb{R}^n : \|\mathbf{x} - \mathbf{y}\|_2 = \|I(\mathbf{x}) - I(\mathbf{y})\|_2. \quad (15)$$

Since isometry preserves distances, it induces the same distance graph. Therefore, graph convexity is invariant to isometries.

Universal scaling is a map $S : \mathbb{R}^n \rightarrow \mathbb{R}^n$ such that

$$\exists C \in \mathbb{R} \quad \forall \mathbf{x} \in \mathbb{R}^n : S(\mathbf{x}) = C\mathbf{x}. \quad (16)$$

It holds that

$$\|S(\mathbf{x}) - S(\mathbf{y})\|_2 = \|C\mathbf{x} - C\mathbf{y}\|_2 = |C| \cdot \|\mathbf{x} - \mathbf{y}\|_2. \quad (17)$$

All the distances are scaled by $|C|$. It follows that the chosen nearest neighbours are the same. We show by contradiction that all the shortest paths are also the same. We denote G the graph with the original edges and G_S the graph with the scaled edges.

Given $\mathbf{x}, \mathbf{y} \in \mathbb{R}^n$, suppose that there exists a shortest path:

$$P = (\mathbf{p}_0 = \mathbf{x}, \mathbf{p}_1, \dots, \mathbf{p}_j = \mathbf{y}) \quad (18)$$

from \mathbf{x} to \mathbf{y} , and a different path:

$$Q = (\mathbf{q}_0 = S(\mathbf{x}), \mathbf{q}_1, \dots, \mathbf{q}_k = S(\mathbf{y})) \quad (19)$$

from $S(\mathbf{x})$ to $S(\mathbf{y})$ such that

$$L(Q) < L(S(P)), \quad (20)$$

where

$$S(P) = (S(\mathbf{p}_0), S(\mathbf{p}_1), \dots, S(\mathbf{p}_j)) \quad (21)$$

and $L(\cdot)$ is an operator measuring the length of a path. From (20), it follows that $C \neq 0$. Because all the edges are scaled by a factor $|C|$, it holds that $L(S(P)) = |C|L(P)$. Moreover, for every pair of nodes $\mathbf{v}_1, \mathbf{v}_2$, there exists an edge in G from \mathbf{v}_1 to \mathbf{v}_2 if and only if there exists an edge in G_S from $S(\mathbf{v}_1)$ to $S(\mathbf{v}_2)$. Hence, there exists a path R from \mathbf{x} to \mathbf{y} such that $Q = S(R)$. It follows that

$$|C|L(R) = L(S(R)) < L(S(P)) = |C|L(P). \quad (22)$$

Therefore, $L(R) < L(P)$ and that contradicts the assumption that P is the shortest path from \mathbf{x} to \mathbf{y} . \square

A.4 Consistency of graph estimates of geodesics

The consistency of sample/graph-based geodesic estimates has been discussed in connection with the introduction of ISOMAP [11] and more generally in [22]. Graph connectivity-based estimates of geodesics from sample data are implemented using two procedures: The neighborhood graph can be determined by a distance cutoff ϵ , so that any points within Euclidean distance ϵ is considered neighbors, or by K-nearest neighbors based on Euclidean distance. Consistency of these estimates, i.e., that the sample-based shortest paths converge to geodesics, is most straightforward to prove for the former approach [11, 22]. The consistency proof for the ϵ -based procedure is based on the smoothness of the metric, a uniformly bounded data distribution ($1/c < p(x) < c$) and scaling of the distance cutoff or K so the connectivity (number of edges per node) increases for large samples (cutoff decays slowly $\epsilon \rightarrow 0$ as sample size $N \rightarrow \infty$) [22]. In finite samples, a (too) large connectivity will bias the geodesics, while a (too) small connectivity can lead to disconnected graphs and noisy estimates.

In pilot experiments, we tested the ϵ and KNN approaches for a range of ϵ and K . We balanced connectivity, stability and bias to adopt a KNN-based approach with $K = 10$ in the complete set of experiments.

B Data sets

B.1 Image domain

We used ImageNet-1k [53, 24] as "classes" in our experiments. The validation set contains 50 images per class. We used "concepts" of two types: texture and colors. Texture data comes from Describable Textures Dataset (DTD)² [19]. It contains 47 textures with 120 images per texture. Color data is a combination of images from [2] and Digikala Products Color Classification.³ We have 9 colors and for each color, we used all images from the Color classification dataset and supplied them with randomly sampled images of the corresponding color from Digikala.

To match the number of concepts and classes and the number of images in each of them, we randomly chose 56 ImageNet classes and 50 images from each concept. In total, we have 2800 "concept" images and 2800 "class" images. We added 5600 images from the validation set of Places365 [44] as "background".

²<https://www.robots.ox.ac.uk/~vgg/data/dtd/index.html>

³<https://www.kaggle.com/datasets/masouduut94/digikala-color-classification>

We used data2vec-base [3] architecture. It consists of 12 Transformer layers [61] and was trained to produce the same representations for an input image and its masked version. It was pre-trained on an unlabelled version of ImageNet-1k. For fine-tuning, one linear layer was added on top of the mean-pooled output of the last layer. Both the pre-trained model⁴ and the model fine-tuned⁵ on ImageNet-1k [53, 24] were obtained from Hugging Face [66]. The details on pre-training and fine-tuning can be found in the original paper [3].

We extracted the input embedding together with 12 layers. For each layer, we averaged the hidden states across patches to get 768-dimensional feature vectors.

B.2 Human activity domain

In the human activity domain, we use the pretrained model from [67] to extract the latent representations. The model is pretrained on a large unlabelled dataset from the UK Biobank, which contains 700,000 person-days of free-living tri-axial accelerometer data. The pretraining procedure is a multi-task self-supervised learning schedule, where the model is trained to predict whether a number of augmentations have been applied or not. The model follows the architecture of ResNet-V2 with 1D convolutions and a total of 21 convolutional layers. The resulting feature vector after the final pretrained layer is of dimension 1024.

The model is divided into 5 modules, 4 modules consisting of 2 ResNet blocks each and a final convolutional layer mapping the data to 1024 channels. We extract the latent representations after each of the 5 modules. Furthermore, during finetuning a classification module consisting of two linear layers is added, and we also extract the features just before the final linear layer. We flatten all of the latent representations.

For testing the methods, we use the Capture-24 dataset [65]. The Capture-24 dataset contains free-living wrist-worn activity tracking data from 152 participants. The participants were tracked for 24 hours and the data was subsequently humanly labelled into 213 categories based on a wearable camera also worn by the participants. Each of the 213 categories is associated with a metabolic equivalent of task (MET) score, which is a number describing the energy expenditure of each task. In [62] the original 213 labels were divided into 4 coarse labels, namely; sleeping, sedentary behaviour, light physical activity behaviours and moderate-to-vigorous physical activity behaviours based on the MET scores. These 4 labels are used as classes when fine-tuning the model. In [65], the authors similarly use the MET score to categorize the original 213 labels, but instead divide them into 11 labels. One of the labels overlaps with the 'sleep' label from the classes and is thus excluded. The remaining 10 labels are used as our concepts.

During finetuning, we randomly select 30 subjects to hold out for testing. We optimize the entire network (encoder and classifier) jointly with a learning rate of 10^{-4} . Following the authors in [67], we select a small validation set and use early-stopping with a patience of 5 epochs. We achieve a balanced accuracy score of 77.8%. We extract the latent representations of the test set both before and after finetuning.

Since all data points are associated with both a label and a concept, the convexity analysis is done separately for classes and concepts. For each concept, we sample 1000 points (or the maximum number available), we then sample 1000 points (or maximum available) from each of the remaining concepts (as well as the class label 'sleep') to use as background. This yields a total of 9139 points. We add 9139 points from the WISDM human activity dataset [64] to the background points. We then analyze the convexity of each concept. We subsequently map all points to their corresponding class and analyze the convexity of each class on the same graph.

B.3 Audio domain

In the audio domain, we use the pretrained wav2vec2.0 model [4], which is trained on the LibriSpeech corpus (960h of unlabeled data) [49]. During pretraining the model learns meaningful latent audio/speech representations, the exact training objectives can be found in [4]. The model consists of a CNN-based feature encoder, a transformer-based context network and a quantization module. We

⁴<https://huggingface.co/facebook/data2vec-vision-base>

⁵<https://huggingface.co/facebook/data2vec-vision-base-ft1k>

are especially interested in the latent space representation in the 12 transformer layers. After each transformer layer, we extract the feature vector of dimension 768.

We fine-tune the model to perform digit classification based on the AudioMNIST dataset [8], which consists of 30000 audio recordings of spoken digits (0-9) in English of 60 different speakers (with 50 repetitions per digit). For fine-tuning an average pooling layer and a linear layer are added to the network, to perform a classification task, the fine-tuning procedure is based on a tutorial⁶. The network is fine-tuned on 80% of the people while the remaining 20% are withheld for testing (resulting in 6000 audio files). The initial CNN layers are frozen, while the transformer layers are fine-tuned. The model is fine-tuned with early stopping for 1000 steps (batch-size 16), and the learning rate is set to $1e^{-4}$. No hyperparameter search was performed as the first fine-tuning already led to a very high accuracy of 99.89%. The latent representations of the test set are extracted before and after fine-tuning.

For the convexity analysis, we compare the latent representations of different classes and concepts. For the AudioMNIST dataset, the classes are the 10 digits. As concepts, we use speaker id, which is provided as metadata of the dataset. Additionally, we transcribe the phonemes of each audio file using "WebMAUS Basic" [56]. The phonemes of each audio are cut into individual audio files and the latent representations are extracted for each phoneme, resulting in 16310 audio files. To evaluate the robustness of the results, relevant background points are added to the dataset, that do not overlap with the classes. In the audio case, the Speech Commands dataset [8] was used to provide these background points. Ten words ('yes', 'no', 'up', 'down', 'left', 'right', 'on', 'off', 'stop', 'go') with 600 repetitions each (matching the data amount of the test set) were randomly chosen from the dataset.

B.4 Text domain

For text, we use the base version of RoBERTa⁷ [43] which is pre-trained to perform Masked Language Modelling [25] in order to reconstruct masked pieces of text. The model consists of an embedding layer followed by 12 transformer encoder layers. The pre-training of RoBERTa is performed on 160GB of uncompressed English-language text in order to learn latent representations of text which are expressed as 768-dimensional vectors.

The GoEmotions dataset [23] is used to provide concepts for texts. The dataset is a filtered collection of texts from reddit.com which are labelled in accordance with the emotions which they express. There is a total of 27 different categories of emotions which are labelled in the dataset. Texts can be annotated with multiple labels and are labelled by multiple times by different annotators. In order to have a simple text-label relationship we only consider a single random instance of an annotation of each text as well as a single label that will define the text's concept. In order to balance and minimize the dataset we only consider a subset of 12 emotions (seen in Figure 3) with an even split between emotions that are associated with positive and negative sentiment. Of this subset, we sample 300 texts from each of the 12 emotions. Additionally, we also include 300 "neutral" texts, which are also labelled in the GoEmotions dataset, to act as background data points for some experiments.

Positive	Negative
excitement, pride, joy, amusement, love, admiration	anger, disgust, sadness, disapproval, nervousness, fear

Figure 3: Selected subset of emotions from the GoEmotions dataset split into their associated class of sentiment

We define the classes of the texts to be a positive or negative sentiment and use texts from the sentiment analysis part of the TweetEval dataset [6, 52] both as data points and for the fine-tuned model⁸ which was obtained from HuggingFace.

⁶https://colab.research.google.com/github/m3hrdadfi/soxan/blob/main/notebooks/Eating_Sound_Collection_using_Wav2Vec2.ipynb

⁷<https://huggingface.co/roberta-base>

⁸<https://huggingface.co/cardiffnlp/twitter-roberta-base-sentiment>

B.5 Medical Imaging domain

We investigate T1w 3T Magnetic Resonance Imaging (MRI) data for gender classification. The data is obtained from the Human Connectome Project S1200 Subjects Release [60]. We use the structurally preprocessed data as described in [36] of 1113 subjects.

We train a self-supervised model using a modified version of the Masked-Auto-Encoder (MAE) [38], a self-supervised model trained on ImageNet for object detection. During pretraining, the Masked-Auto-Encoder takes a subset of patches as input and aims to reconstruct the full input image. The model uses a patch-embedding layer with fixed position encoding, a transformer-based encoder and decoder block as well as a linear layer for reconstruction. As the encoder receives only a subset of patches, masked patches are introduced to the model after the encoder block. In our case, the model is modified to take a subset of 3d volumes as input. Instead of adding a fixed sine-cosine position-encoding, positional encoding is learned by the model. For finetuning, we omit the decoder and attach a single classification layer and train the model on the full input volume.

We use MONAI [16] as the implementation framework. The input data is of shape $256 \times 256 \times 256$ voxels and is evenly divided into 512 subvolumes of shape $32 \times 32 \times 32$ voxels. The 512 subvolumes are flattened and randomly masked out using a masking ratio of 75% resulting in an input tensor of shape 128×32^3 . The embedding dimension is set to 768 and 512 for the encoder and decoder blocks respectively. Our pretrained model is trained on 667 subjects for in total 700 epochs and a learning rate of 0.0008 with a linear warm-up and a cosine-decay [16]. We define the Mean-Squared-Error between the ground truth image and reconstruction of masked patches as loss, equivalent to [38]. Validation loss does not increase during pretraining. We use the same data for pretraining and finetuning. For finetuning, we train for 30 epochs with a learning rate of 0.0001 and a cosine decay and use binary-cross-entropy as loss for gender prediction. The optimal validation loss is reached after only 5 epochs with a classification accuracy of 82%.

As for the other modalities, we define both class labels and concepts. We use anatomical brain regions as concepts and gender as class labels. To define brain regions, the original segmentation mask consisting of many cortical and sub-cortical regions is downsampled to 13 distinct major regions: White Matter, Ventricles, Cerebellum, Thalamus, Caudate, Putamen, Pallidum, Brain-Stem, Hippocampus, Amygdala, Accumbens, Corpus, Callosum and Cortex. To obtain the feature vector \mathbf{v} for a particular concept c in layer l , we calculate the weighted sum over all embedding vectors \mathbf{z}_j over the subvolume j , such that

$$\mathbf{v}_{l,c} = \sum_{j=1}^J w_{c,j} \mathbf{z}_{l,j}, \quad (23)$$

where $w_{c,j}$ is the ratio of voxels labelled with concept c in subvolume j and the total number of voxels in j and $\sum_{j=1}^J w_{c,j} = 1$.

To retrieve the feature vector \mathbf{v}_i for the class label gender in layer l , we calculate the mean over all subvolumes, i.e. $w = \frac{1}{J}$ in Equation 23. For a total of N subjects, this results in $N \times (13 + 2)$ feature vectors for 13 concepts and 2 classes.

For the convexity analysis, we sample 200 subjects for each class and concept, none of which are used in pretraining or fine-tuning. Additionally, we sample 200 background points from subjects used in validation during pretraining and fine-tuning. Therefore, class and concept points in the foreground can not originate from the same subject, however, they will likely lie within the convex regions of foreground classes and concepts.

C Detailed Results

C.1 Image domain

We show tSNE plots for a subset of classes and concepts (Figure 11) of the image domain. Even though the pretrained model has never seen the labels, it clusters both classes and concepts toward the end of the network. As expected from Theorem 1, the fine-tuned model clearly separates the classes in the last layer. Figure 11 shows that color concepts are mostly clustered in the input layer, whereas

texture concepts get more clustered toward the end of the model. The "background" points are well mixed with both concepts and classes, so they are relevant for our tests.

Figure 6a shows the convexity analysis with included background points. A comparison of Figure 6b and Figure 6a suggests that the graph convexity scores are robust to the number of points in the graph not belonging to any class nor concept. We notice that the convexity of classes increases throughout the network. The convexity of concepts initially increases but decreases in the second half of the model. The scores for both concepts and classes increase after fine-tuning, even though we do not fine-tune to recognize concepts.

Figure 16 shows hubness metrics (k-skewness and Robinhood score) for both models. It follows that hubness is not a problem in the image domain, except for the last layer of the fine-tuned model.

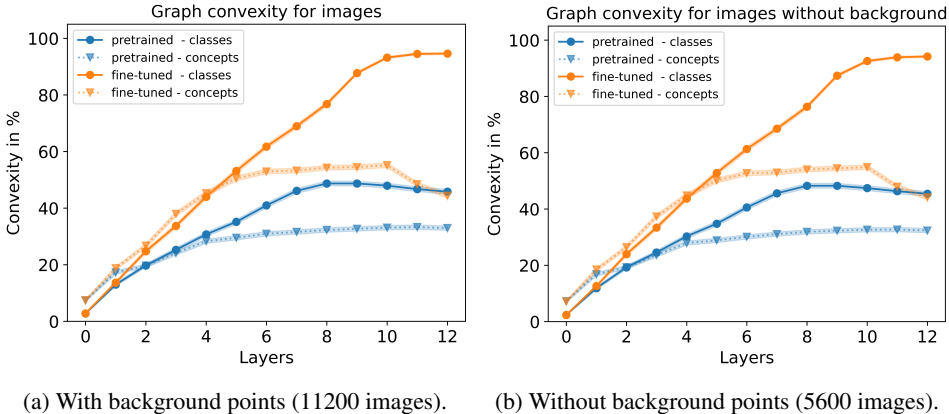


Figure 6: Graph convexity in the image domain.

C.2 Human activity domain

Figure 12 shows the tSNE plots with the classes and concepts of the human activity domain. The figure shows the tSNE plots of the representations after the first, third, and last (sixth) layers for both the pre-trained and the fine-tuned model. For both the pre-trained and fine-tuned model, it is clear that the class separation increases throughout the network. Thus, in the first layer, all points seem to be located on the same manifold, whereas already in the third layer, the *sleep* class is well separated from the remaining classes. In the last layer of the fine-tuned model, the *light* class looks to be less clustered compared to the remaining classes. Furthermore, both the *moderate-vigorous* class and the *sedentary* class points are located in multiple clusters.

Throughout the network, the concepts become increasingly clustered. In the final layer, concepts such as *bicycling* and *vehicle* are clearly separable from the remaining concepts, while concepts such as *sitstand+activity* and *walking* appear more scattered. Overall, the tSNE plots all indicate that the pre-trained model already is able to distinguish between the classes and concepts. However, fine-tuning does contribute to a higher separability of classes and concepts.

Figure 16 shows the hubness measures for the human activity models before and after finetuning. We notice that the plots do show some degree of hubness, especially in the first layers. However, in both the pre-trained and fine-tuned model, the hubness measures decrease to rather small values for the final layers.

Figure 7a shows the convexity analysis for both the pre-trained and fine-tuned networks in the human activity domain. In both models, we notice a clear pattern of increasing convexity between the first and the last layer for both classes and concepts. Both the class and concept convexity increase after fine-tuning (although only slightly). The increase in convexity of concepts indicates that the concepts are helpful for classification. The concept convexity of the final layer increases from 42.9% to 46.9%, whereas the class convexity increases from 66.0% to 69.4% between pretraining fine-tuning.

In Figure 7b the convexity analysis is repeated but without background points. The plots show a similar overall pattern, although the numbers themselves are slightly higher (final concept convexity of 47.7% and class convexity of 71.5% after fine-tuning).

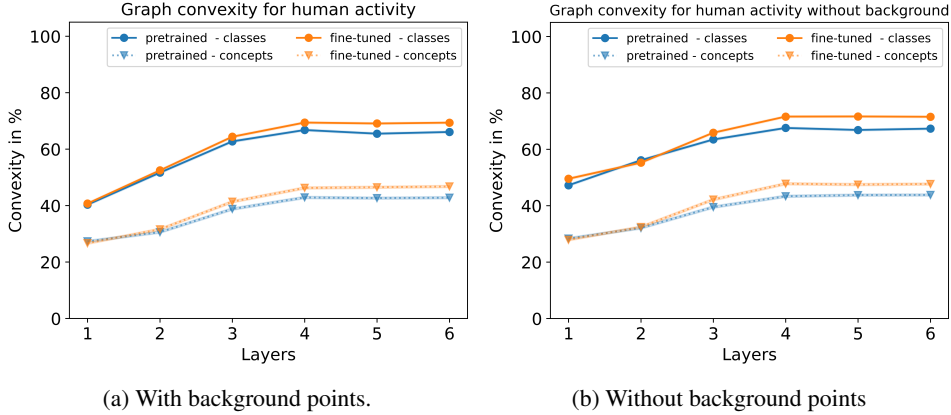


Figure 7: Graph convexity in the human activity domain.

C.3 Audio domain results

Figure 13 shows the tSNE plots for classes and concepts in the audio domain. The clustering of classes can be seen in late layers in both the pre-trained and fine-tuned model, although it’s more pronounced in the fine-tuned model. This is as expected from Theorem 1. The concept phonemes also forms clusters to some extent, most prominent in the early to middle layers of the network.

This observed behavior is also reflected in the convexity analysis through shortest paths (Figure 8a), where the convexity generally increases for the classes trough out the layers and the convexity of the concept phonemes decreases in the second half of the network. Interestingly, the convexity of phonemes increases with fine-tuning while the convexity of speaker-id decreases with fine-tuning, as already discussed in Section 3.1.

The presence of background points does not influence the results strongly. The curve shapes are very similar with and without background points as can be seen in Figure 8a and Figure 8b, just the exact values vary a little.

The hubness analysis (Figure 16) shows low values of k-skewness (<1.1) and of the Robinhood score (<0.27) in both models for all layers, so we did not need to correct for this in the convexity analysis.

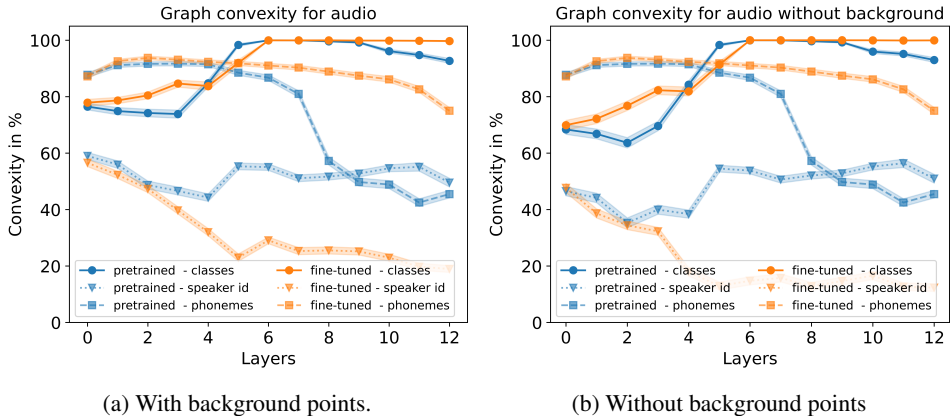


Figure 8: Graph convexity in the audio domain.

C.4 Text results

In the tSNE plots in Figure 14, we see that a separation between the emotions according to their associated sentiment clearly occurs in the later layers of the fine-tuned model. Given the dataset’s inherent ambiguity in that one sentence can carry multiple labels of emotions we don’t expect a perfect separation of classes.

For hubness metrics in Figure 16 we immediately notice that the shape of the Robinhood score differs significantly from the pre-trained model to the fine-tuned one.

For the graph convexity Figure 9a we notice that there is a slight increase in the proportion for the concepts suggesting that the emotion concepts are more convex after fine-tuning on sentiment. It is also apparent that this change only shows in the later layers of RoBERTa.

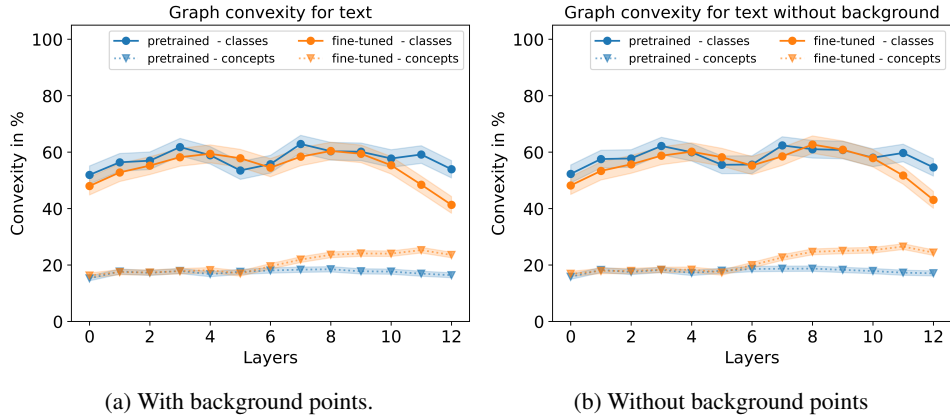


Figure 9: Graph convexity in the text domain.

C.5 Medical Imaging Results

In Figure 15 we show TSNE plots for the pretrained and finetuned model for both classes and concepts. To be consistent with the other domains regarding background points, we also include 200 randomly sampled class or concept points used for validation during training and define them as background. The classes overlay less after fine-tuning compared to pretraining. However, some distinctions can be seen before fine-tuning. Furthermore, some structures can be observed in the concepts. Figure 10a shows graph convexity for the pretrained and finetuned model for both classes and concepts. It can be seen that class convexity increases after fine-tuning, whereas concept convexity decreases.

Figure 10b shows the same metric as Figure 10a without background points. Here, convexity is slightly smaller. That is because background points do not differ in any way from concepts or classes defined as foreground and do lie within the convex regions of the foreground. As a result, convexity increases when removing background points.

Convexity does not change much after the second layer. Layer zero holds the learned position embeddings and patch embeddings, whereas layers one to six are transformer blocks. It seems that these layers are very similar, and one does not gain much information in regard to classes and concepts when progressing through the encoder layers beyond one.

Skewness and Robinhood scores shown in Figure Figure 16 show low values (max. ≈ 1.5 for k-Skewness and max. ≈ 0.25 for Robinhood scores). Convexity was therefore not corrected for hubness.

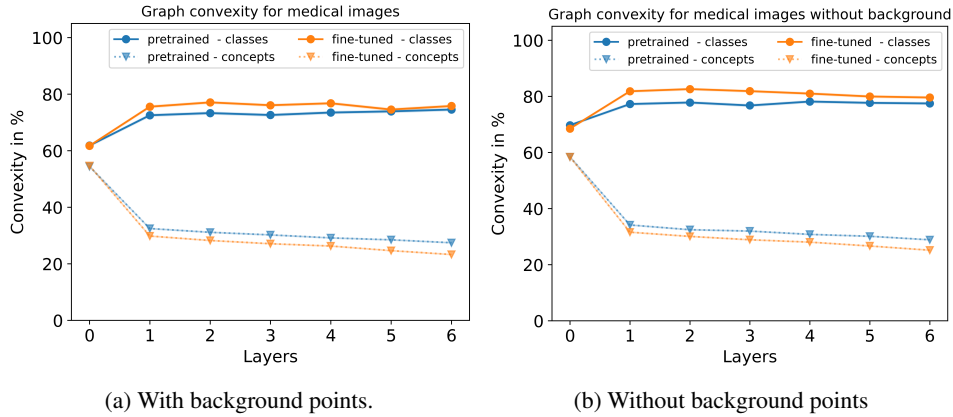


Figure 10: Graph convexity per layer in the medical image domain for the pretrained (blue) as well as fine-tuned model (orange). Class convexity (circles) increases after fine-tuning, whereas concept convexity (triangles) decreases. Removing background points results in a slight decrease in class convexity, whereas it does not change concept convexity.

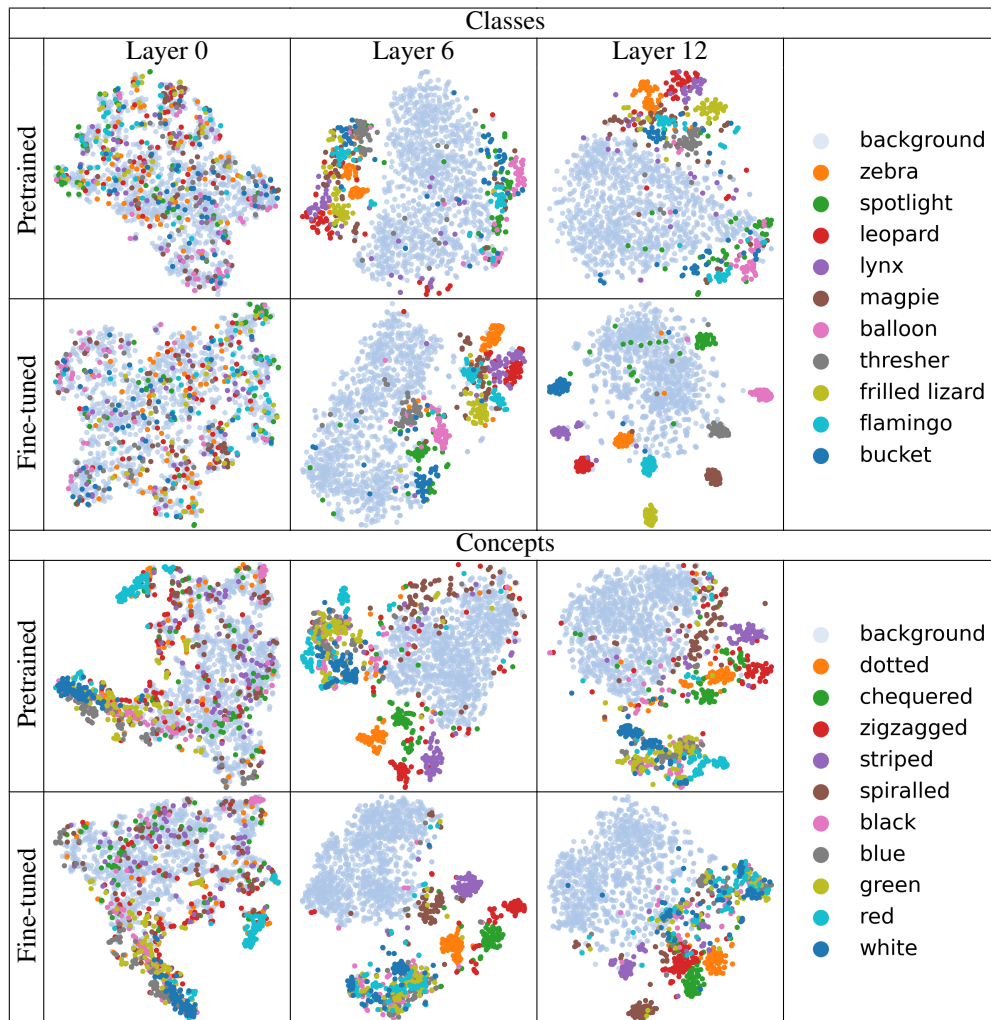


Figure 11: Images: t-SNE plots for a subset of classes (top) and concepts (bottom), with 50 images per concept or class and 1000 background points, both before and after fine-tuning.

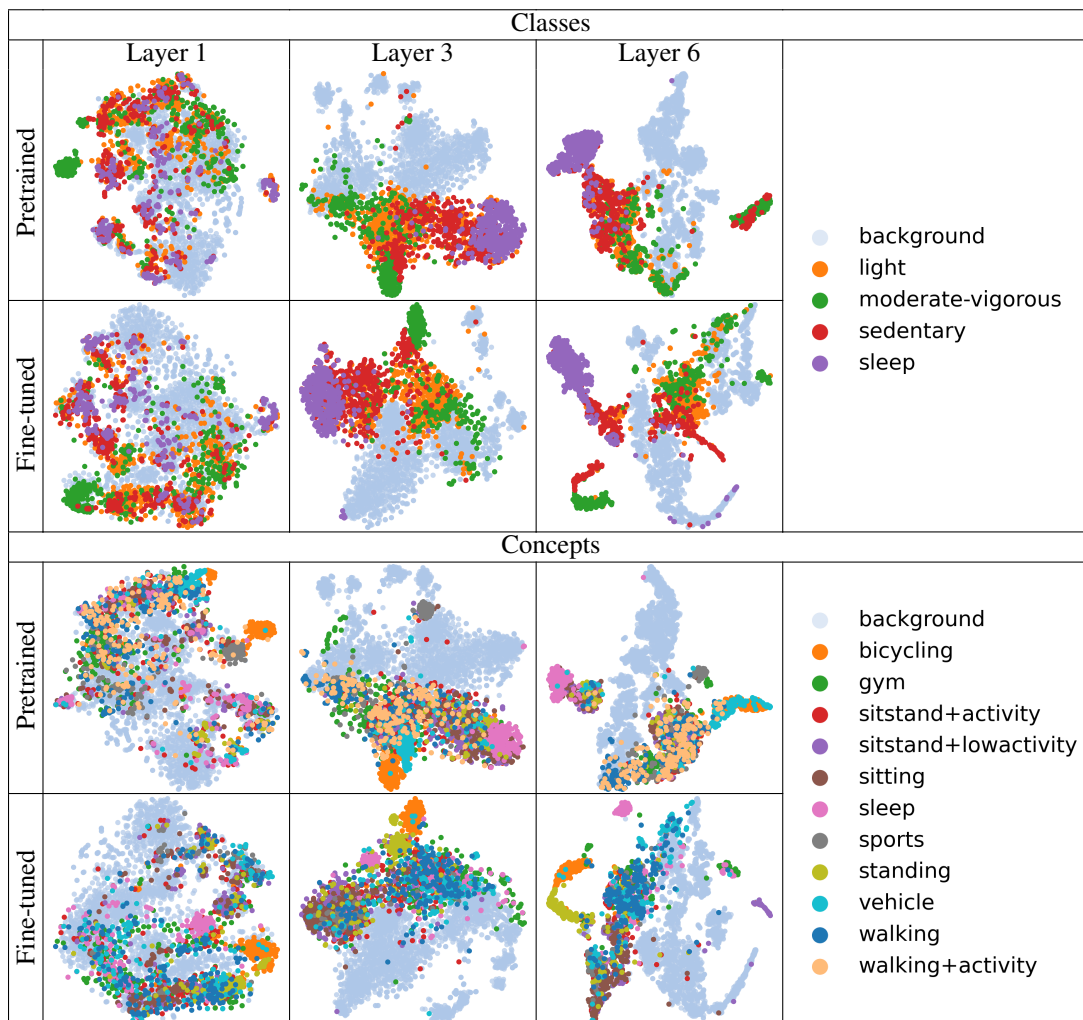


Figure 12: Human activity: t-SNE plots for a subset of classes (top) and concepts (bottom), both before and after fine-tuning.

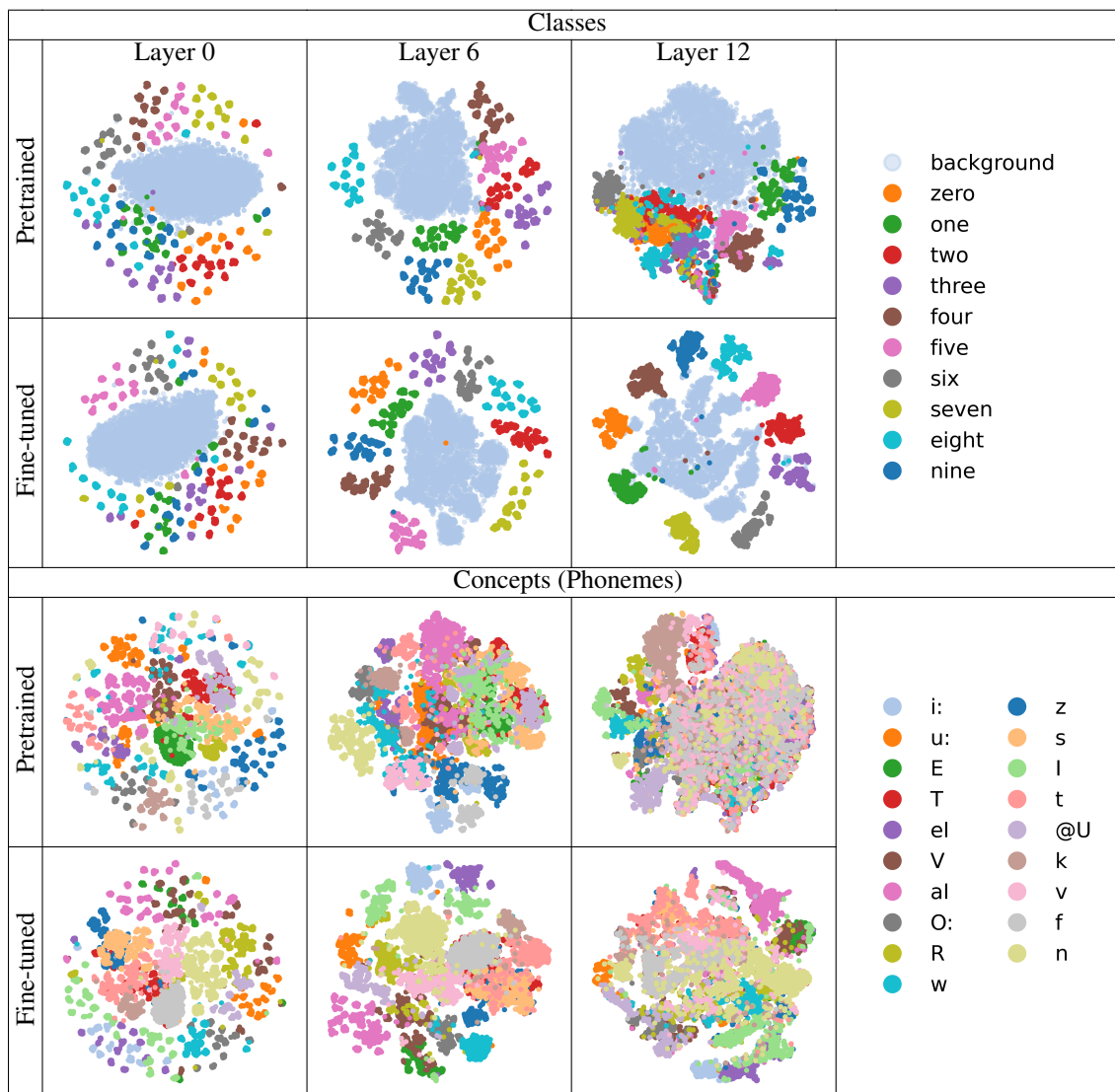


Figure 13: Audio: t-SNE plots for classes (top) and phonemes (bottom), both before and after fine-tuning. For the classes 600 points per class and 6000 background points are shown, for the phonemes a total of 16310 points are shown.

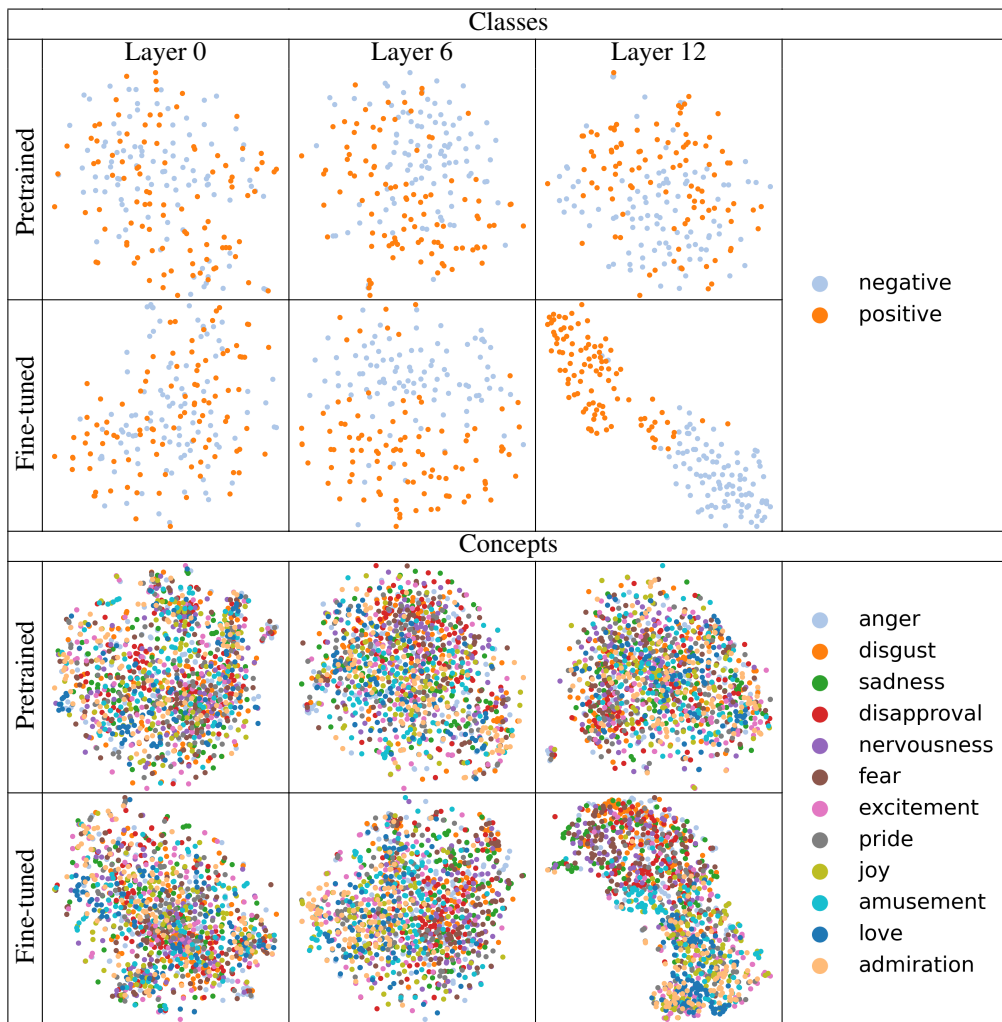


Figure 14: Text: t-SNE plots for a subset of classes (top) and concepts (bottom), with 100 texts per concept or class both before and after fine-tuning.

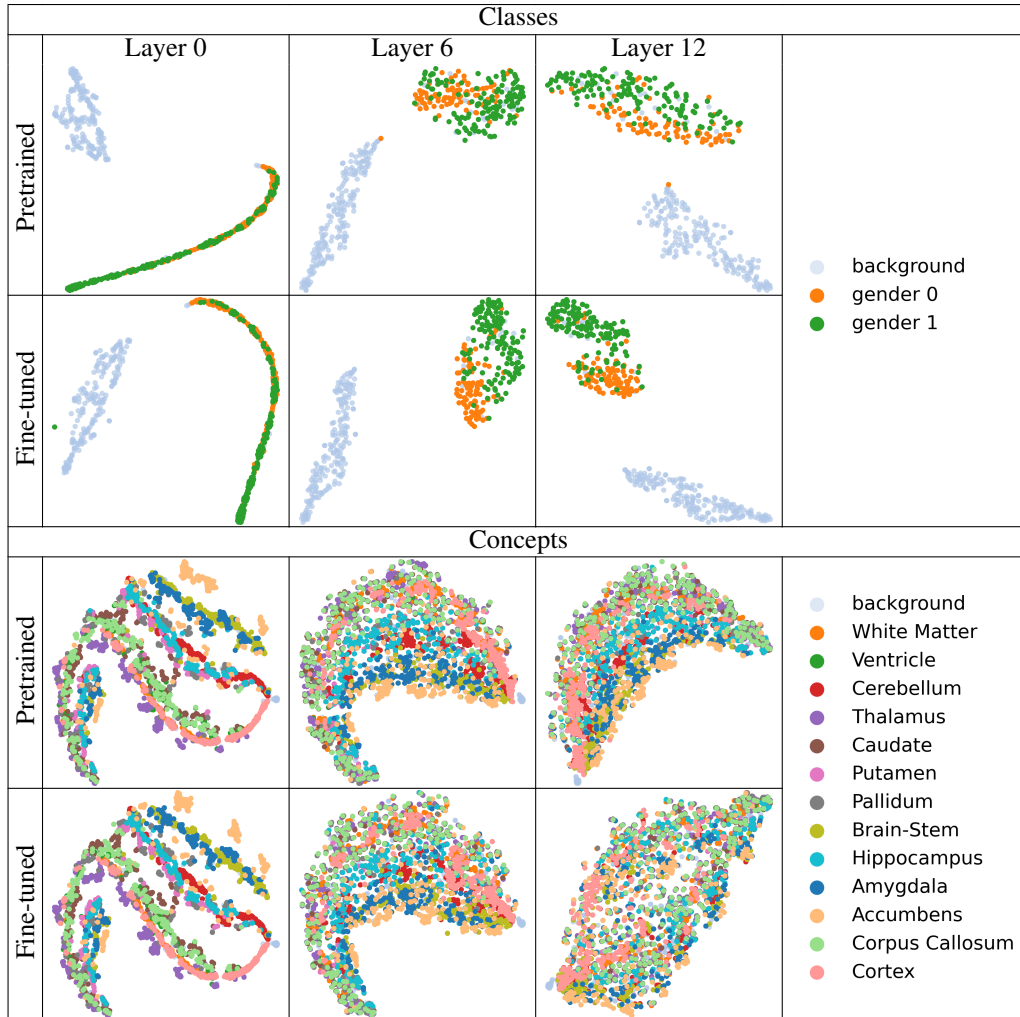


Figure 15: Medical images: t-SNE plots for a subset of classes (top) and concepts (bottom). The plot shows 200 foreground points per concept and class, as well as 200 background points. Background points were randomly sampled and originate from a different sample than those used in the foreground.

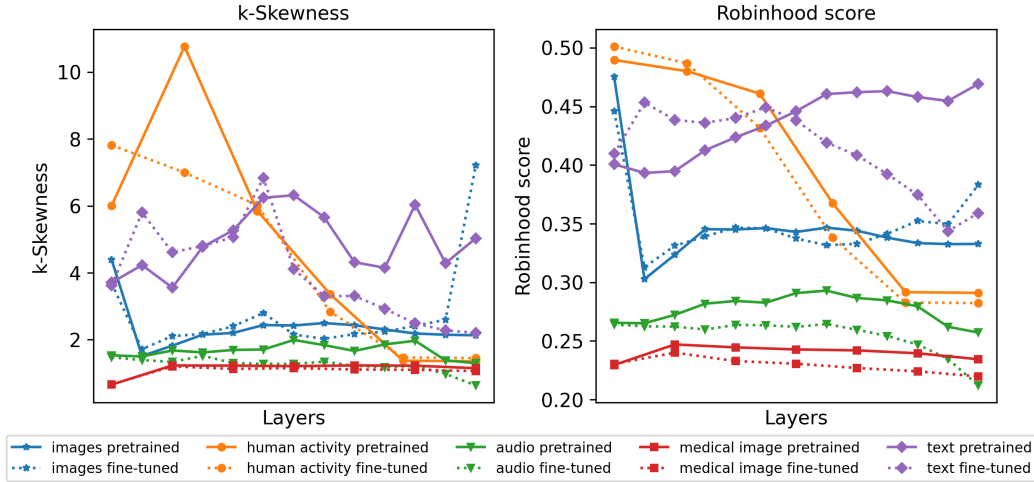


Figure 16: Hubness evaluation for all modalities. No measures to correct for hubness were taken, as the numbers for k-skewness and Robinhood score are generally low.

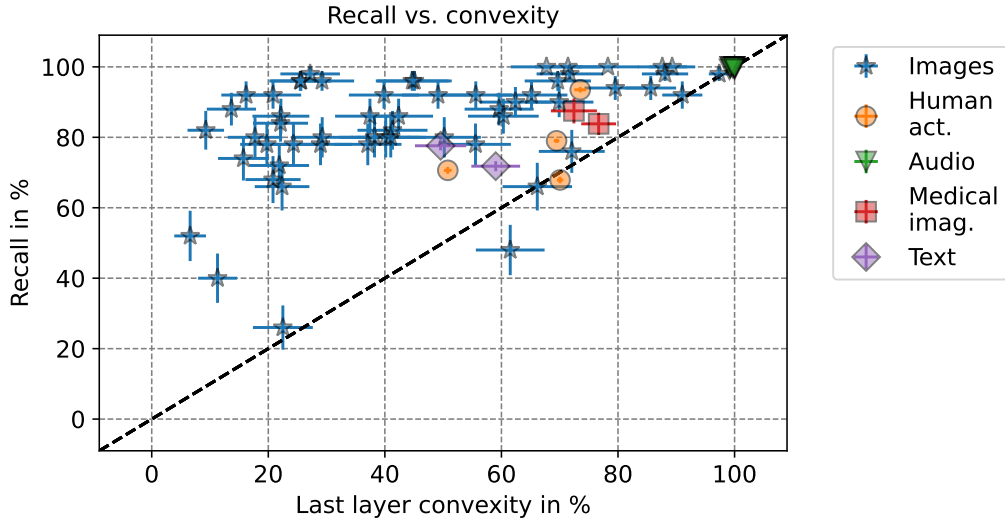


Figure 17: Convexity of a subset of classes in the pretrained models vs. recall of these classes in the fine-tuned models for all data domains with error bars. The error bars show the standard error of the mean for the recall and the adjusted version of the standard error of the mean for the convexity. Note that the results were rerun for this figure and therefore look slightly different compared to Figure 5 in the main paper. The correlation coefficient is 0.54.

C.6 Recall vs. convexity

Figure 17 shows the recall vs. convexity plot with error bars included. The error bars are computed using the standard error of the mean for both the recall and the adjusted version of the standard error of the mean for the convexity. The results were rerun for this plot and are thus slightly different compared to Figure 5 in the main paper. However, the overall trend is still the same, and we have a correlation coefficient of 0.54 between pretraining convexity and fine-tuning recall. The uncertainties for convexity are higher than in the other plots with graph convexity results because the adjusted standard error of the mean is computed for each class, therefore, n is much smaller than if we compute it for all classes at once (especially in the image domain where we have many classes).